Observations of the Structure and Evolution of Hurricane Edouard (2014) during Intensity Change. Part II: Kinematic Structure and the Distribution of Deep Convection

ROBERT F. ROGERS

NOAA/Atlantic Oceanographic and Meteorological Laboratory/Hurricane Research Division, Miami, Florida

JUN A. ZHANG

NOAA/Atlantic Oceanographic and Meteorological Laboratory/Hurricane Research Division, and Cooperative Institute for Marine and Atmospheric Studies, Rosenstiel School for Marine and Atmospheric Sciences, University of Miami, Miami, Florida

JONATHAN ZAWISLAK AND HAIYAN JIANG

Florida International University, Miami, Florida

GEORGE R. ALVEY III AND EDWARD J. ZIPSER

University of Utah, Salt Lake City, Utah

STEPHANIE N. STEVENSON

University at Albany, State University of New York, Albany, New York

(Manuscript received 7 January 2016, in final form 31 May 2016)

ABSTRACT

The structural evolution of the inner core and near-environment throughout the life cycle of Hurricane Edouard (2014) is examined using a synthesis of airborne and satellite measurements. This study specifically focuses on differences in the distribution of deep convection during two periods: when Edouard intensified toward hurricane status, and when Edouard peaked in intensity and began to weaken. While both periods saw precipitation maximized in the downshear-left and upshear-left quadrants, deep convection was only seen from the aircraft during the intensifying period.

Deep convection was located farther inside the radius of maximum winds (RMW) during the intensifying period than the weakening period. This convection is traced to strong updrafts inside the RMW in the downshear-right quadrant, tied to strong low-level convergence and high convective available potential energy (CAPE) as the storm remained over warm water in a moist environment. Strong updrafts persisted upshear left and were collocated with high inertial stability in the inner core. During weakening, no deep convection was present, and the precipitation that was observed was associated with weaker convergence downshear right at larger radii, as CAPE was reduced from lower sea surface temperatures, reduced humidity from subsidence, and a stronger warm core. Weak updrafts were seen upshear left, with little coincidence with the high inertial stability of the inner core.

These results highlight the importance of the azimuthal coverage of precipitation and the radial location of deep convection for intensification. A more symmetrical coverage can occur despite the presence of shear-driven azimuthal asymmetries in both the forcing and the local environment of the precipitation.

1. Introduction

This study continues an examination of the intensity change of Hurricane Edouard (2014), a storm in which the National Oceanic and Atmospheric Administration

Corresponding author address: Robert Rogers, NOAA/AOML/Hurricane Research Division, 4301 Rickenbacker Causeway, Miami, FL 33149.
E-mail: robert.rogers@noaa.gov

DOI: 10.1175/MWR-D-16-0017.1

(NOAA) WP-3D and G-IV, as well as National Aeronautics and Space Administration (NASA) unmanned Global Hawk, provided detailed measurements of the environment and inner core over several days of its life cycle as part of the NOAA Intensity Forecasting Experiment (IFEX; Rogers et al. 2013a) and NASA Hurricane Severe Storm Sentinel Experiment (HS3; Braun et al. 2016). This unique sampling offers an opportunity to investigate the environmental-, vortex-, and convective-scale processes that govern tropical cyclone (TC) intensity change. Zawislak et al. (2016, hereafter Part I) focused on Edouard's vortex-scale thermodynamic changes, as revealed in high-altitude dropsonde observations from the Global Hawk, in relation to the precipitation evolution using data from infrared and passive microwave sensors. Part II describes the kinematic and precipitation structure in more detail during Edouard's near-rapid intensification on 14 September and near-peak intensity after weakening begins on 16 September, exploring possible mechanisms that can explain the radial, azimuthal, and temporal distribution of deep convection and its influence on intensity change.

Previous studies have shown that the structure and distribution of inner-core precipitation is an important determinant of TC intensification. Satellite-based studies (e.g., Jiang 2012; Kieper and Jiang 2012; Zagrodnik and Jiang 2014; Tao and Jiang 2015) have noted that it is primarily the azimuthal distribution of shallow and moderate convection (defined by echo tops in the lower and middle troposphere) that distinguishes TCs about to undergo significant intensification. In contrast to these studies, airborne, modeling, and other satellite-based studies have focused on deep convection (defined here as echo tops above 14 km collocated with strong updrafts in the upper troposphere) as a key indicator of TCs undergoing intensification (e.g., Kelley et al. 2004; Hendricks et al. 2004; Braun et al. 2006; Montgomery et al. 2006; Reasor et al. 2009; Guimond et al. 2010; Rogers et al. 2013b, 2015; Stevenson et al. 2014; Susca-Lopata et al. 2015). The apparent contradiction regarding the importance of shallow/moderate versus deep convection may be attributable to the fact that many of the airborne datasets (e.g., those shown in Rogers et al. 2013b, 2015), consist primarily of TCs already undergoing intensification, after the intensifying secondary circulation has had time to develop deep convection, while the satellite studies have a large number of cases prior to the onset of intensification, when low-level forcing mechanisms are likely important in the development of shallow/moderate convection (Tao and Jiang 2015). It may also result from differences in how the timing of the onset of intensification is defined. Efforts to reconcile these apparently different conclusions are ongoing.

In terms of deep convection, a preferred radial and azimuthal distribution in the inner core has been identified as more favorable for intensification. For the radial distribution, a preponderance of deep convection inside the radius of maximum winds (RMWs) is favorable for intensification, since diabatic heating in the region of high inertial stability and upper-level subsidence around the periphery of the convective outflow preferentially warms the region inside the RMW (Shapiro and Willoughby 1982; Schubert and Hack 1982; Nolan et al. 2007; Vigh and Schubert 2009; Pendergrass and Willoughby 2009; Rogers 2010; Zhang and Chen 2012; Chen and Zhang 2013; Rogers et al. 2013b, 2015; Susca-Lopata et al. 2015). Radial inflow in the lower troposphere can establish regions of enhanced convergence, particularly in the planetary boundary layer (PBL), which have been shown to be preferred regions for the initiation of convection (Rogers et al. 2013b, 2015; Miyamoto and Takemi 2015). The outer-core distribution of lower-tropospheric inertial stability may impact the radial profile of convergence, since higher inertial stability provides a greater resistance to radial parcel displacements and a reduced mass flux to the inner core. Rogers et al. (2015) showed this relationship by comparing lower-tropospheric inertial stability between an intensifying and a steady-state TC. Finally, differences in slope between the updraft surfaces and angular momentum surfaces, reflective of the tangential wind field and intensity of the convection, helps determine whether or not the peak diabatic heating in the convection remains inside the high-inertial stability environment within the RMW (Hazelton et al. 2015; Rogers et al. 2015).

The azimuthal distribution of deep convection and its relationship with intensification focuses mostly on its distribution relative to the environmental vertical shear vector. Vertical shear has long been identified as playing a key role in modifying TC structure and intensification. Shear often results in a tilted vortex and associated thermal, kinematic, and precipitation asymmetries. These asymmetries include a negative (positive) lower- (upper-) tropospheric temperature anomaly and enhanced lower-tropospheric inflow and ascent downshear, and a precipitation maximum downshear and downshear left (e.g., Jones 1995; DeMaria 1996; Bender 1997; Frank and Ritchie 2001; Black et al. 2002; Corbosiero and Molinari 2003; Rogers et al. 2003; Braun et al. 2006; Wu et al. 2006; Reasor et al. 2009; Reasor and Eastin 2012; Reasor et al. 2013; Dolling and Barnes 2014).

In terms of intensification, shear has been hypothesized to weaken TCs through midlevel ventilation of dry air (Riehl and Malkus 1961; Emanuel et al. 2004; Tang

and Emanuel 2010). DeMaria (1996) argued that tilting of the vortex in shear would result in a more stable stratification in the midtroposphere, weakening convection in the eyewall and weakening the storm. Shear can also impact TC intensification through forcing of convection at and outside the RMW on the downshear side, which reduces θ_E in the PBL of the inflow and weakens convection in the eyewall (Riemer et al. 2010; Molinari et al. 2013; Zhang et al. 2013). In contrast to the above-mentioned detrimental impacts of vertical shear on TC intensification, Cram et al. (2007) described an exchange of high-θ_E air between the eye and eyewall in the low levels on the downshear left side that replenished the downdraft-cooled air. The TCs can also intensify in the presence of moderate shear through forcing of strong convection downshear with a strong symmetric projection (Nguyen and Molinari 2012) and sometimes downshear reformation (Molinari et al. 2004, 2006; Molinari and Vollaro 2010; Nguyen and Molinari 2015).

The shear-relative azimuthal distribution of precipitation has also been identified as being important in TC intensity change. A key distinction between intensifying and nonintensifying TCs is the presence of deep convection in the upshear-left (USL) quadrant (Stevenson et al. 2014; Zagrodnik and Jiang 2014; Onderlinde and Nolan 2014, 2016; Rogers et al. 2015; Chen and Gopalakrishnan 2015; Alvey et al. 2015). Deep convection in the upshear quadrants provides a greater projection of diabatic heating onto the symmetric mode, a configuration that is more efficient at spinning up the vortex (Nolan et al. 2007; Jiang 2012). If the convection is associated with a midlevel vortex that is also located upshear of the low-level vortex, then advection of this midlevel feature by the mid- to upper-level flow can also lead to vortex alignment and intensification (Stevenson et al. 2014).

While a symmetric distribution of convection and diabatic heating is preferable for intensification, the forcing for that convection can be asymmetric, either due to frictional asymmetries arising from storm translation (e.g., Shapiro 1983; Kepert 2001; Kepert and Wang 2001) or vertical shear (see citations above). Using airborne radar, Black et al. (2002) showed a preferred region of low-level convergence on the downshear side of Hurricanes Jimena (1991) and Olivia (1994). Barnes and Dolling (2013) used GPS dropsondes to show a persistent wavenumber-1 structure to inflow consistent with what would be expected given the shear and motion of Hurricane Humberto (2001). Reasor et al. (2013) used composites of airborne Doppler data from multiple cases to show that the deepest layer of convergence is in the downshear-right quadrant. DeHart et al. (2014), using a similar composite methodology, found that convection initiates downshear right, intensifies downshear left, and weakens upshear left. A similar evolution of convective structure in a tilt-relative framework (which can be related to the vertical shear) was found in simulations of Hurricane Bonnie (1998) in Braun et al. (2006). From these studies, it is clear that the structure and evolution of the thermodynamic and kinematic fields of TCs in sheared environments play an important role in governing the distribution of inner-core deep convection and TC intensity evolution. In contrast to the asymmetries in inflow depth and strength from these studies, Sitkowski and Barnes (2009) showed that the inflow of Guillermo (1997) became nearly axisymmetric as it underwent RI.

Observations of these relationships that span the entire troposphere have been limited, however. The Halverson et al. (2006) study was one that did show a comprehensive analysis of the warm core structure of Hurricane Erin (2001), using primarily high-altitude dropsondes to assess the structure and evolution of the vortex in the presence of vertical shear. Many of the structures mentioned above, including the distribution of deep convection, are found in Halverson et al. (2006). However, this data only spans one day and does not include information on the three-dimensional kinematic structure that can be provided by airborne Doppler measurements.

Part I of this two-part case study provided a synoptic overview of Edouard and relates the vortex-scale thermodynamic changes Edouard experienced to the precipitation evolution described using data from infrared and passive microwave sensors. In addition to mean thermodynamic profiles from each Global Hawk flight, which emphasized the importance of moistening and humidification of the middle troposphere in the initially drier upshear regions of the inner core, a detailed analysis was also provided for two typically undersampled periods in Part I: one early when Edouard was slowly intensifying as a weak tropical storm, and the other when Edouard was rapidly dissipating under high vertical wind shear and relatively low sea surface temperatures. Part II of this study describes a 2-day period (between those two periods analyzed in Part I), in which Edouard was intensifying to peak intensity and another day when it was beginning to weaken from that peak. Using the airborne Doppler radar from the NOAA P-3 aircraft, combined with Global Hawk and P-3 dropsondes and lightning flash counts as detected by the World Wide Lightning Location Network (WWLLN; Lay et al. 2004; Stevenson et al. 2014), this part focuses on the kinematic structure of the storm and the distribution of deep convection, as well as the conditions that

govern its radial and azimuthal distribution. These conditions include both the kinematic structures shown here and the thermodynamic structures shown in Part I.

2. Aircraft sampling and datasets used

As discussed in Part I, multiple NOAA and NASA aircraft flew missions within and around Edouard between 12 and 19 September. Part II focuses on the coincident AV6/NOAA43 missions on 14 and 16 September, when Edouard was steadily intensifying (14 September) and beginning to weaken after peak intensity (16 September). Figure 1 shows the flight tracks of the aircraft sampling Edouard during these two days. On 14 September NOAA43 flew a figure-4 pattern followed by a series of eyewall penetrations on the northeast side of the inner core (not shown). AV6 flew a combination of a lawnmower survey pattern during the first half of its mission, followed by a butterfly-type storm-relative pattern during the second half of its mission. On 16 September NOAA43 flew a repeated series of eyewall passes, while NOAA42 flew a partial figure-4 pattern followed by a series of spirals while deploying the low-altitude Coyote unmanned aerial system (not shown). Only NOAA43 is considered for this day. During this time AV6 flew a rotating butterfly pattern for its entire mission, providing extensive azimuthal coverage with its ~500-km radial legs centered on the storm.

In addition to the dropsondes and WWLLN lightning flash counts used in Part I, Part II features three-dimensional analyses of wind and reflectivity from the airborne Doppler radar on the P-3. The analyses use a variational method (Gamache 1997; Reasor et al. 2009) to obtain grids with a 2 km × 2 km horizontal and a 0.5-km vertical spacing. The individual radial passes, which generally take ~1 h to complete, are merged into a single analysis that represents the conditions of the vortex over the time scale of the flight pattern (~3 h for these missions). The merged analyses are sufficient for the depiction of more slowly evolving vortex-scale parameters that require greater spatial coverage (e.g., azimuthally averaged fields and horizontal flow). For the smaller-scale and more rapidly evolving convective-scale fields, individual radial passes are used. A similar analysis approach was followed in Rogers et al. (2012, 2013b, 2015).

3. Vortex-scale structure and distribution of deep convection

Figure 2 shows the Doppler-derived storm-relative winds at 2- and 8-km altitude for the NOAA43 missions on 14 and 16 September. The 2-km RMW is ~30 km on

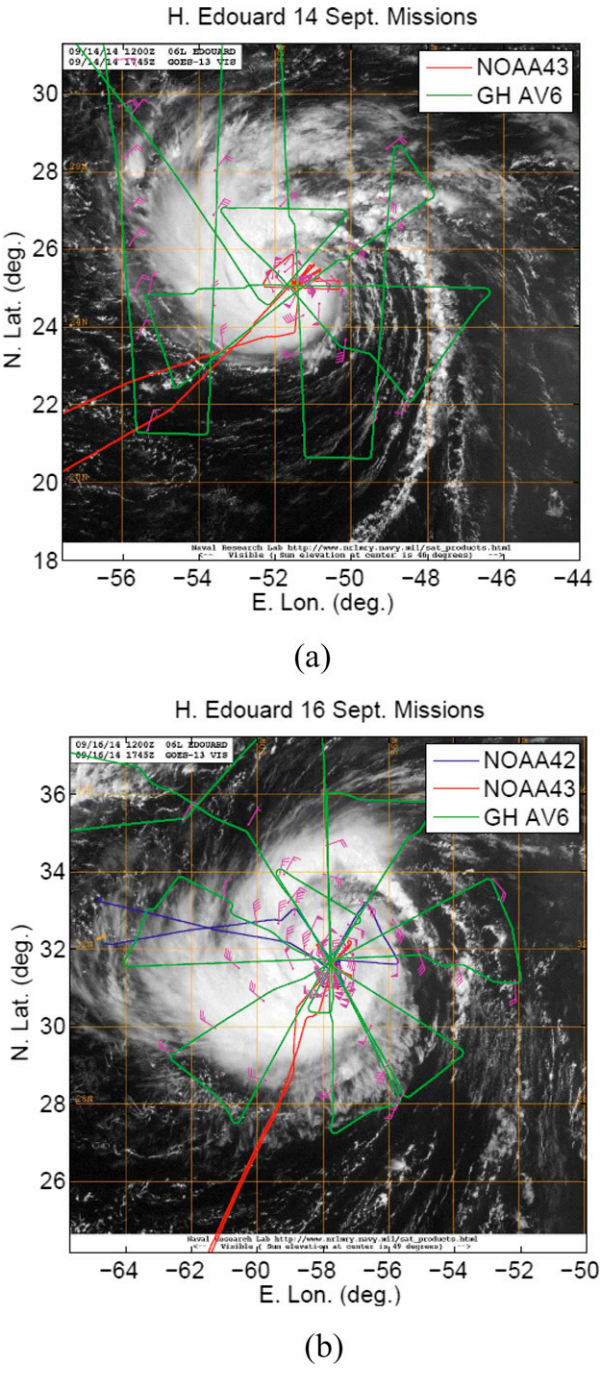

FIG. 1. *GOES-13* visible satellite images, aircraft flight tracks, and near-surface dropsonde measurements for 14 and 16 Sep in Edouard. Flight tracks are shown in a translating storm-relative coordinate system. Blue line denotes flight track of NOAA42, red line NOAA43, and green line GH AV-6. (a) Visible image valid at 1745 UTC 14 Sep; (b) visible image valid at 1745 UTC 16 Sep.

both days. The intensification of the storm between the two days is evident, with peak winds increasing from 35 m s^{-1} on 14 September and expanding to a broader area of >40 m s^{-1} winds on 16 September. A visual

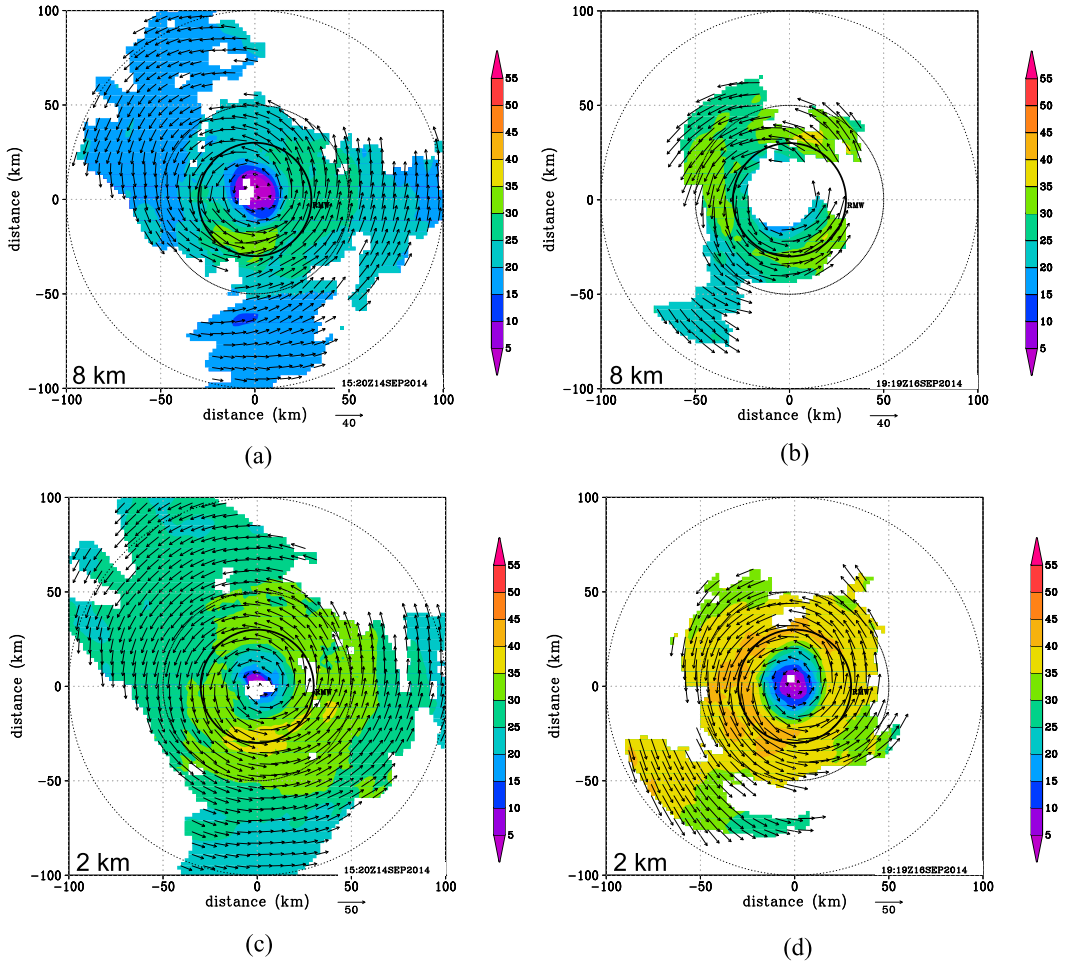

FIG. 2. (a) Doppler-derived storm-relative wind speed (shaded, m s^{-1}) and flow vectors (m s^{-1}) at 8-km altitude for the 14 Sep mission. (b) As in (a), but for the 16 Sep mission. Thick circle in both plots denotes location of RMW at 2-km altitude. (c) As in (a), but for winds at 2-km altitude. (d) As in (c), but for the 16 Sep mission.

inspection of the 8-km flow on 14 September indicates that, unlike on 12 September (cf. Part I), the displacement of the circulation centers between the lower and upper levels is greatly reduced. However, there is still an indication of a small (<5 km) displacement at 8 km toward the northeast on this day. The 8-km flow on 16 September also indicates a displacement, this time toward the northwest with a magnitude of ~5 km. While these values may seem small, they are nonetheless ~10%–15% of the RMW, which can establish asymmetries in radial flow fields due to the displacement of the circulation centers between levels. Reasor and Eastin (2012) used dual-Doppler radar observations to document the tilt structure and evolution of Hurricane Guillermo (1997). As in the present case, the 2–7-km center displacements were small compared to the RMW scale and only 1–3 multiples of an analysis grid cell. While they recognized that some fluctuations (over a 4–5-h period) in tilt structure from one analysis to the next could be nonphysical and artifacts of the methodology, the consistent general orientation of the tilt agreed with previous numerical and theoretical studies. Reasor and Eastin (2012) also highlighted how local measures of center (like the center of circulation) are reflective of the more resilient vortex core, whereas measures that account for the tilt of the broader-scale vortex (like vorticity centroid) often indicate substantially larger values of tilt. The fact that a displacement of the circulation centers was seen in Edouard (Reasor and Eastin did not in the case of Guillermo) is likely physically significant. Despite this tilt, however, Edouard steadily intensified on 14 September in the presence of light-to-moderate (~6 m s^{-1}) shear (cf. Fig. 2 from Part I), reaching peak intensity by 16 September under similar values of shear.

A plot of reflectivity from the lower-fuselage (LF) radar on NOAA43 for both 14 and 16 September is

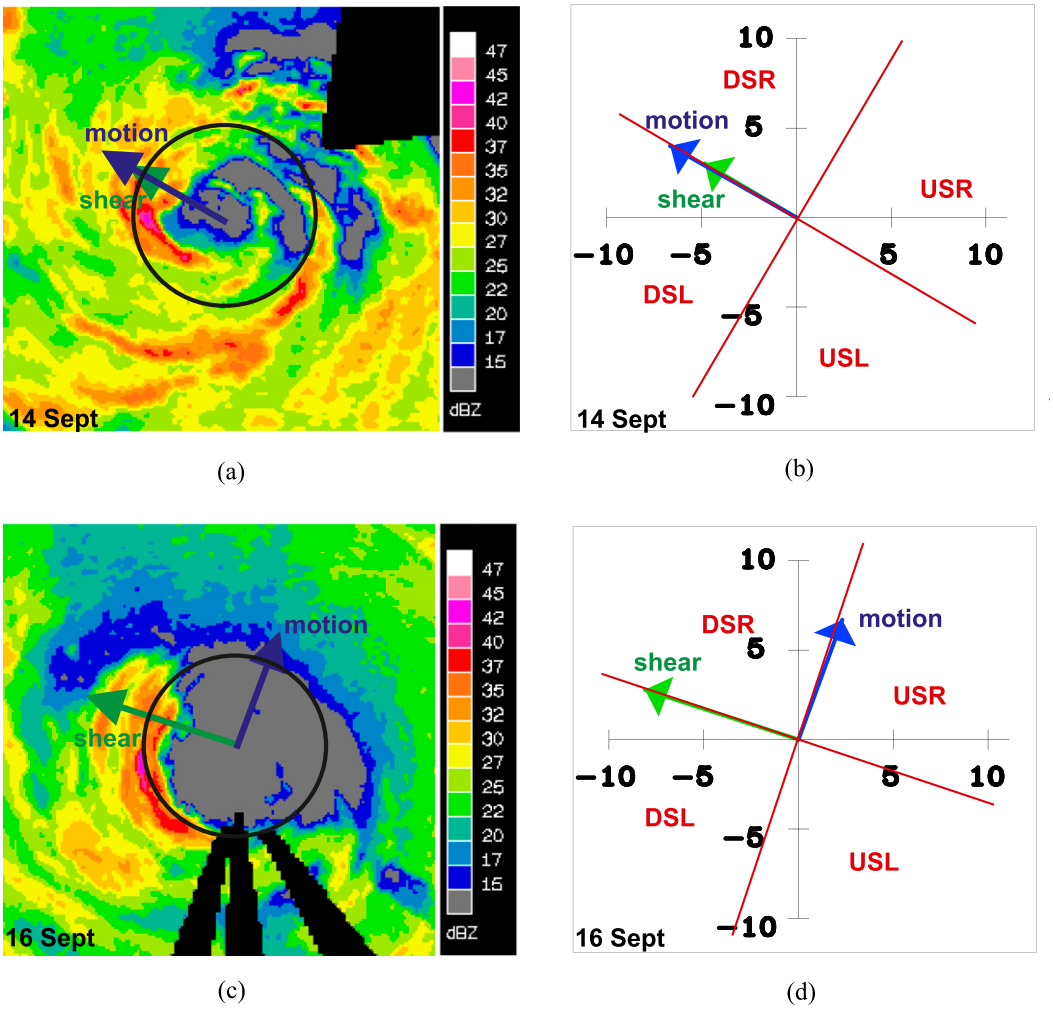

FIG. 3. (a) Storm-centered lower-fuselage plot of reflectivity (shaded, dBZ) at ~2.5-km altitude from a single sweep taken at 1746 UTC 14 Sep. Domain is 144 km on a side. Storm motion (blue arrow) and SHIPS-derived 850–200-hPa shear vectors (green arrow) overlain on radar image. (b) Storm motion (blue arrow, m s^{-1}) and SHIPS-derived 850–200-hPa shear vectors (green arrow, m s^{-1}) for 1800 UTC 14 Sep, with quadrants denoting downshear left (DSL), downshear right (DSR), etc., indicated. (c) As in (a), but for 2124 UTC 16 Sep. (d) As in (b), but for 1800 UTC 16 Sep. The circles in (a) and (c) denote approximate location of 2-km RMW.

shown in Fig. 3. Both days contain a maximum in reflectivity on the southwest side of the eyewall; however, 14 September has a more widespread distribution of reflectivity at other locations around the storm. On the contrary, the eastern eyewall is essentially devoid of precipitation on 16 September (note that the apparent reflectivity on the north, northeast, and east side of the image in Fig. 3c is sea clutter and is thus spurious). With respect to shear orientation, the location of the maximum LF reflectivity is primarily found to the left of the shear vector both days (cf. Figs. 3b and 3d). Most of the high reflectivity is located in the downshear-left (DSL) quadrant, but some precipitation is also found in the USL, particularly on 14 September.

While the LF images provide information on the horizontal distribution of reflectivity, they do not provide any information on its vertical structure, an important component to infer locations of deep convection. Figure 4 shows plots of the echo top (defined as the height of the 20-dBZ surface) and peak vertical velocity in the 8–16-km layer from individual passes of the tail Doppler radar on 14 and 16 September. On 14 September, a ~25 km × 25 km area of deep convection in the southwest (SW) side of the eyewall (DSL and USL) has maximum echo tops exceeding 16 km. Elsewhere in the domain the only other echoes reaching 10-km altitude are a small area ~80–100 km from the center on the west side of the storm. The strongest upward

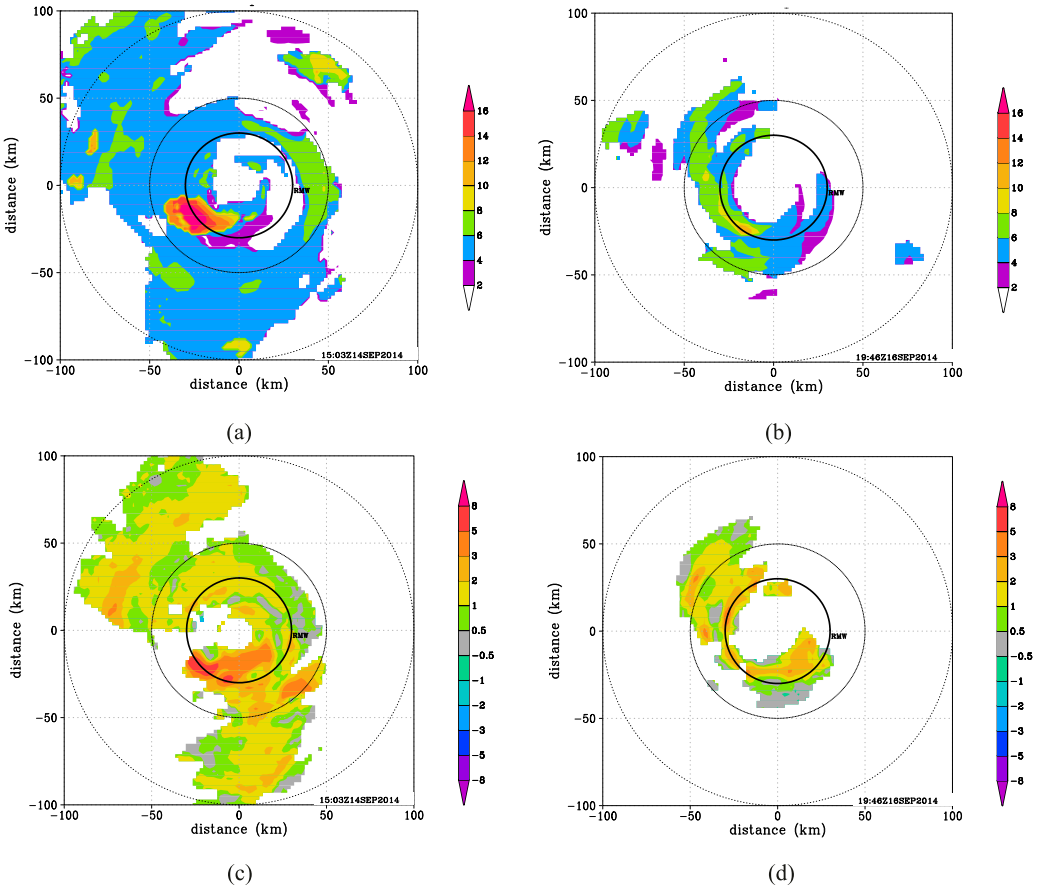

FIG. 4. (a) Height of the 20-dBZ echo top (shaded, km) from tail Doppler radar during center pass at 1503 UTC 14 Sep. Range rings marked every 50 km; RMW indicated by thick black circle. (b) As in (a), but for center pass at 1946 UTC 16 Sep. (c) As in (a), but for peak vertical velocity (shaded, m s^{-1}) in the 8–16-km layer. (d) As in (c), but for the 1946 UTC 16 Sep pass.

motion in the upper troposphere approaches 8 m s^{-1}, coincident with the highest echo tops. In contrast, the pass on 16 September (Fig. 4b) shows that the maximum echo tops are only 12 km. A very small region of echo tops >10 km is observed on the SW (i.e., DSL, USL) side within an otherwise broad region of echo tops between 6 and 8 km. Consistent with this reduced echo-top height, the peak updrafts during the pass are <5 m s^{-1}, with only limited, isolated areas exceeding 3 m s^{-1}.

The center passes shown in Fig. 4 clearly demonstrate differences in the distribution of deep convection on 14 and 16 September, with a larger amount of higher echo tops and stronger updrafts on 14 September compared with 16 September. However, Fig. 4 only shows one pass for each flight. A more comprehensive depiction of the distribution of deep convection is shown in Fig. 5, which presents locations in the Doppler analysis where the peak 8–16-km vertical velocity exceeds 3 and 5 m s^{-1} for all center passes during the 14 and 16 September missions, normalized by the RMW at 2-km altitude. A broad region of updrafts >3 and 5 m s^{-1}, generally at and inside the low-level RMW, is concentrated in the DSL and (especially) the USL quadrants on 14 September. A significant amount of the strongest updrafts are located in the 0.5–0.75 × RMW band. Such a radial distribution of deep convection is consistent with intensifying TCs as shown in Rogers et al. (2013b, 2015), Stevenson et al. (2014), and Susca-Lopata et al. (2015). Contrary to 14 September, 16 September has a much smaller region of grid points >3 m s^{-1}, primarily found in the DSR and DSL quadrants, with a very small area found USL. For the most part these updrafts are found at and just inside the low-level RMW; however, no updrafts >5 m s^{-1} are observed, a result consistent with the lack of high echo tops for 16 September shown in Fig. 4.

An additional depiction of the spatial and temporal variation of deep convection during the approximate times of the NOAA43 missions on 14 and 16 September can be seen in Fig. 6, which shows the distribution of

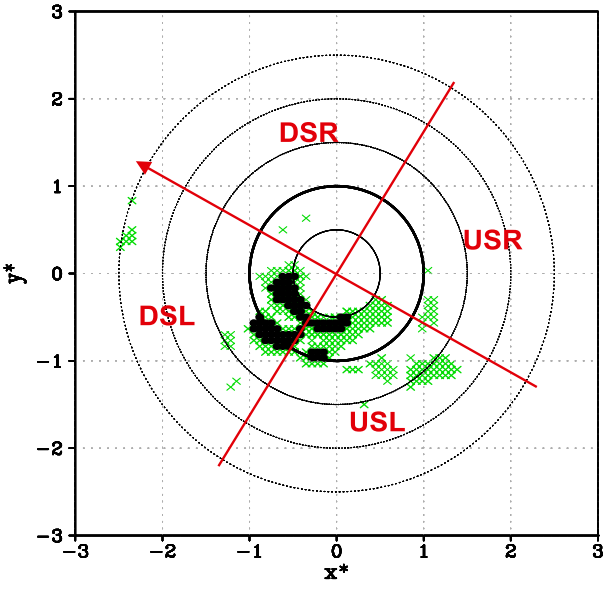

(a)

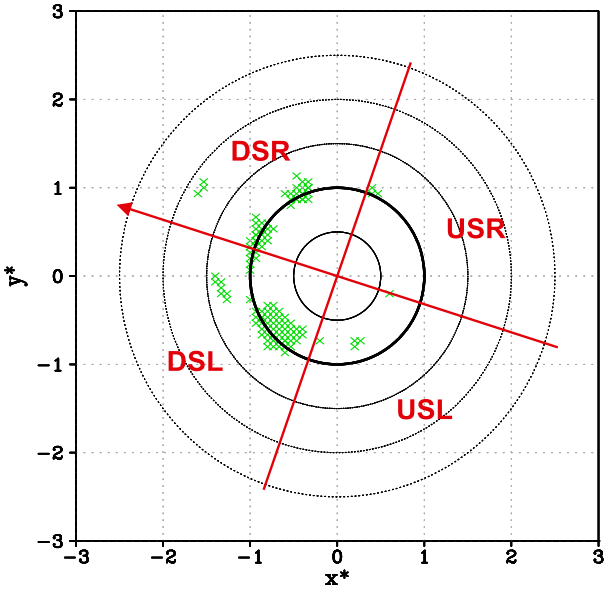

(b)

FIG. 5. (a) Locations of all points in Doppler analysis in a radial coordinate system normalized by the 2-km RMW (x^*, y^*) where peak upward motion in the 8–16-km layer is greater than 3 m s^{-1} (green ×s) and 5 m s^{-1} (black dots) for all center passes during the 14 Sep mission. (b) As in (a), but for the 16 Sep mission. Arrow denotes shear direction; shear-relative quadrants are labeled.

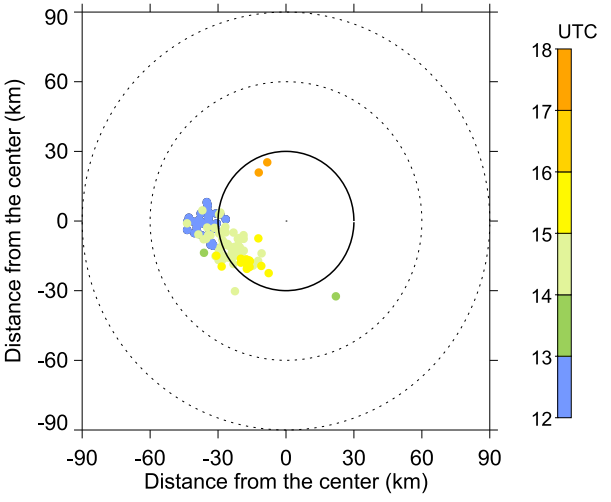

(a)

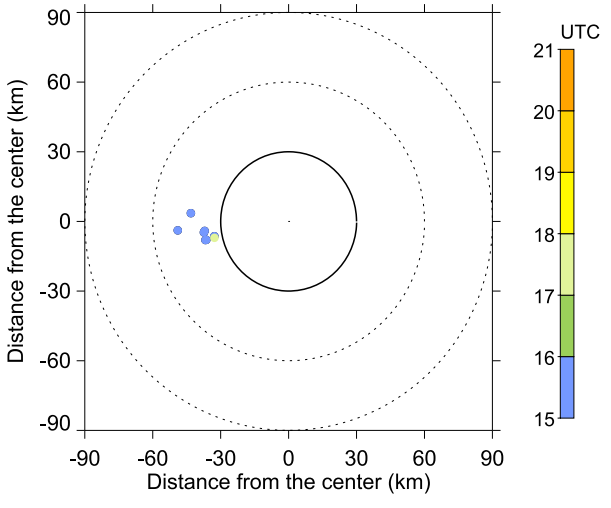

(b)

FIG. 6. Location of lightning flashes as detected by WWLLN every hour between (a) 1200 and 1800 UTC 14 Sep and (b) 1500 and 2100 UTC 16 Sep. Range rings are every 30 km. Lightning strikes are Earth relative (i.e., they are not rotated relative to the shear vector). Thick black circle denotes RMW.

lightning flash counts from WWLLN during a 6-h window that includes the times the aircraft was in the storm. Lightning flashes on 14 September (Fig. 6a) are seen initially between 1200 and 1300 UTC in the DSL quadrant. Over the next 3 h, flashes reach the USL quadrant [similar to what was seen in Hurricane Earl; Stevenson et al. (2014)] and are located inside the 2-km RMW. The flashes during 1500–1600 UTC correspond well with the high echo tops and strong upper-level upward motion seen in the 1503 UTC center pass shown in Fig. 4. Some lightning flashes occur during 16 September, but these are much less numerous, and outside the RMW, compared to 14 September.

The azimuthal and vertical structure of precipitation and vertical motion during the two flights can be seen in Fig. 7, which shows reflectivity and vertical motion

averaged in a 15-km radial ring between r = 15 and 30 km (i.e., just inside the 2-km RMW). While the resolution of the radar analyses, the averaging technique, and the length of time (~3 h) needed to survey the entire storm all preclude a detailed investigation of the structure and evolution of individual convective elements, important information on the azimuthal variation of the basic precipitation structure around the storm can be obtained. On 14 September there is a region of high reflectivity DSR near the melting level, coincident with upward motion in the lowest 4 km. This reflectivity becomes a clear maximum in lower-tropospheric reflectivity downwind, on the west and south sides of the storm (i.e., left of the shear vector). Additionally, high reflectivity extends to a high altitude (near 16 km) in the DSL and USL quadrants. This high reflectivity is coincident with strong upward motion above 8-km altitude in the DSL and particularly USL quadrants. Underneath this region of strong upper-level upward motion USL is a region of pronounced subsidence, extending from ~8-km down to 1–2-km altitude. This shear-relative azimuthal variation in precipitation is similar to that shown in Black et al. (2002), Braun et al. (2006), and DeHart et al. (2014). The azimuthal distribution on 16 September shows many similarities to 14 September, including the precipitation maximum left of the shear vector and low-level upward motion DSR. However, one clear difference is a relative lack of high reflectivity at high altitudes, particularly USL. While there is an indication of upward motion aloft and subsidence below USL, it is much weaker on 16 September than 14 September.

As Figs. 3–7 indicate, the majority of the precipitation and deep convection is located in the DSL and USL quadrants for both days. However, the precipitation can be traced back to the shear-relative quadrants upwind. For example, Fig. 8 shows LF images at ~10–25-min intervals for a ~1.5-h period on 14 September. The letters "A" and "B" denote trackable locations of reflectivity cores (or groups of cores) from LF animations. While convection can be seen in all quadrants at different times, in general it follows a pattern of developing, strengthening and consolidating, and dissipating in specific quadrants. For example, beginning at 1628 UTC, a group of three reflectivity cores (A) is evident in the USR and DSR quadrants (Fig. 8a). These cores translate through the DSR and into the DSL quadrant over ~30 min, at which point they merge into a single large core by 1700 UTC. At the same time another small core develops near the boundary of the USR and DSR quadrants (B in Fig. 8d). This core is also tracked around the storm, reaching its largest size by 1722 UTC as it passes through the DSR and into the DSL quadrant (the same time that A has begun to dissipate). The B core remains coherent for the next 20–25 min, where it is clearly seen in the DSL and USL quadrants by 1745 UTC. This sequence of events describes a typical evolution of the reflectivity cores—initiation at the

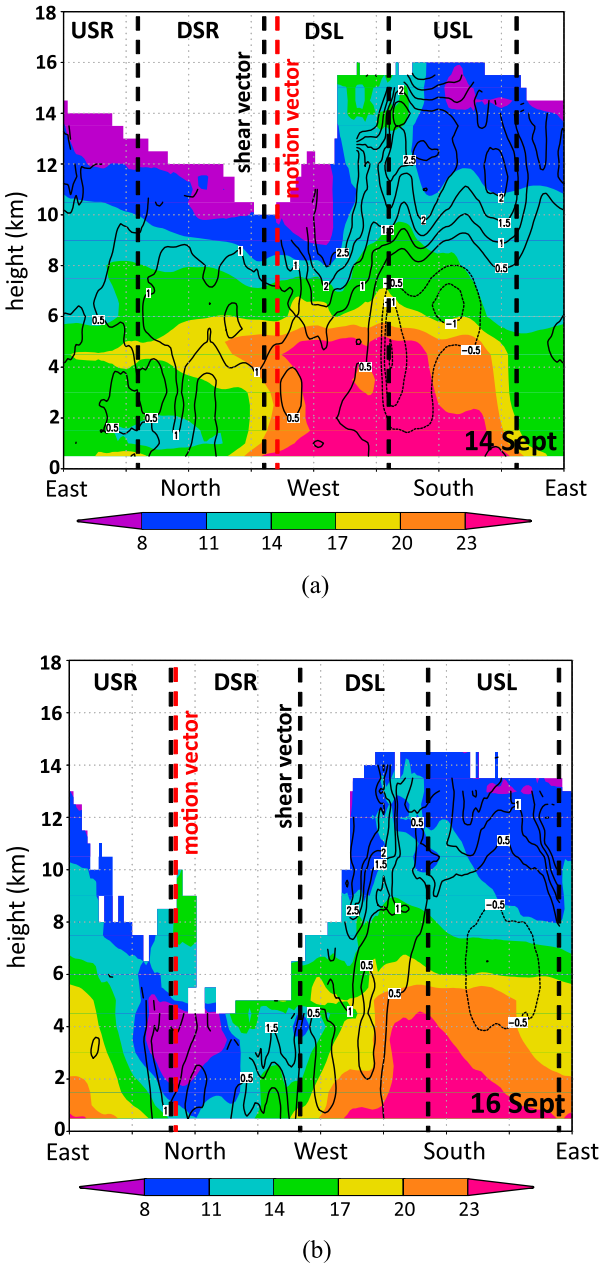

FIG. 7. (a) Azimuth–height plot of reflectivity (shaded, dBZ) and vertical velocity (contour, m s^{-1}) averaged in the r = 15- to r = 30-km radial band for the 14 Sep mission. Direction of storm motion (shear) labeled and indicated by red (black) dashed lines. "East," "north," etc. labels refer to Earth-relative locations. Shear-relative quadrants as indicated in Fig. 6 are labeled. (b) As in (a), but for the 16 Sep mission. In both plots, a minimum of 40% coverage is required before the field is plotted.

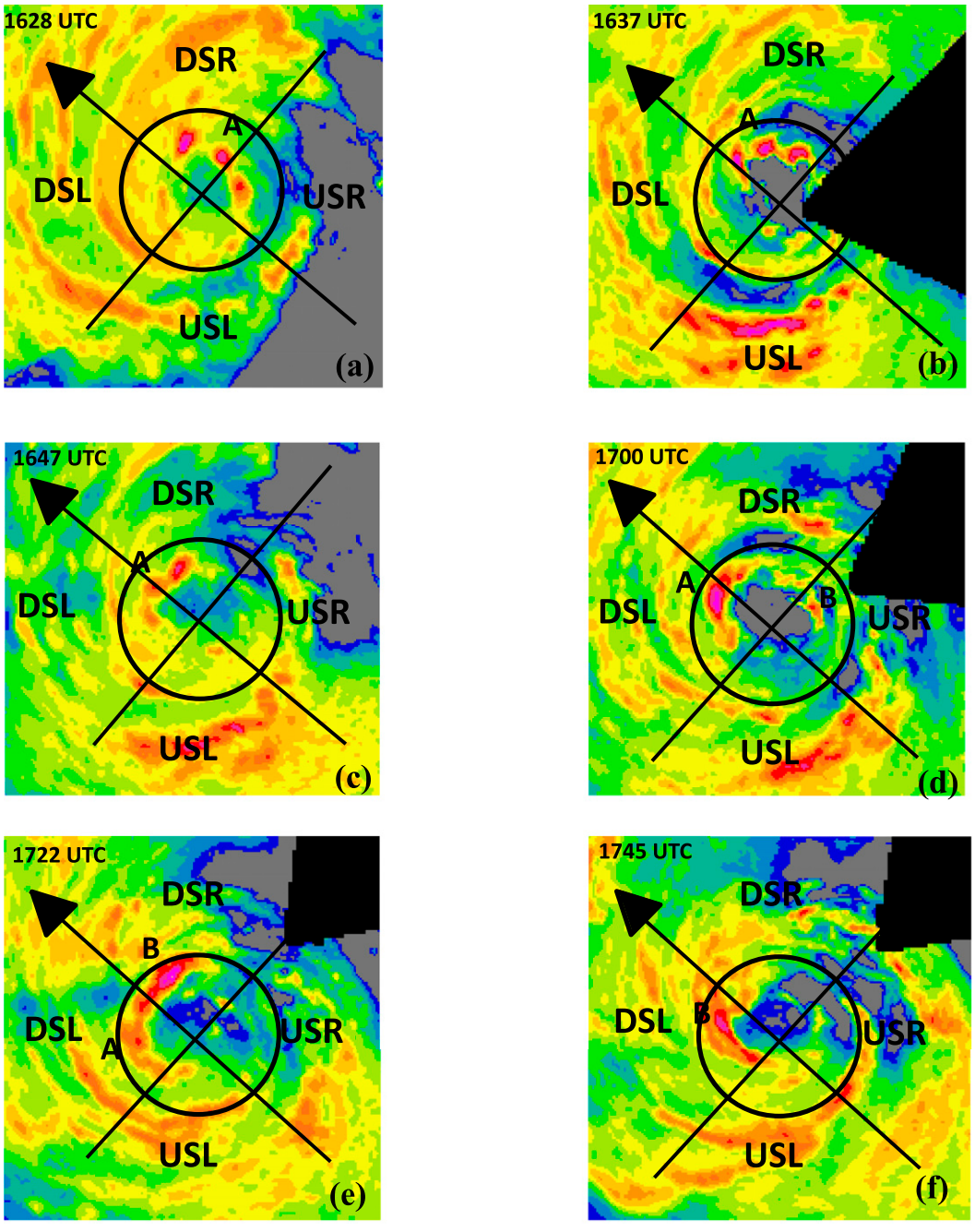

FIG. 8. Storm-centered lower-fuselage plot of reflectivity (shaded, dBZ) at ~2.5-km altitude from a single sweep taken during missions 140914I1 at (a) 1628, (b) 1637, (c) 1647, (d) 1700, (e) 1722, and (f) 1745 UTC. Domain is 144 km on a side. Letters "A" and "B" denote individual reflectivity cores (or groups of cores) trackable with lower-fuselage animations. Circle denotes approximate location of 2-km RMW.

USR/DSR quadrant boundary, intensification in the DSR quadrant, consolidation in the DSL quadrant, and maturation (and in some cases dissipation) in the USL quadrant—a result similar to that described in Black et al. (2002), Braun et al. (2006), and DeHart et al. (2014). This azimuthal evolution of the reflectivity cores is similar on 16 September (not shown). However, the vertical structure of the precipitation, as manifested by the radial and azimuthal distribution of deep convection (cf. Figs. 4–7), reveals differences between the two periods. Specifically, the presence of deep convection on 14 September, including in the USL quadrant,

distinguishes that intensification period from the weakening period on 16 September, when there was limited deep convection DSL, and a lack of convection USL.

4. Mechanisms underlying distribution of deep convection

a. Azimuthal distribution

This section will discuss some mechanisms controlling the distribution of deep convection and the likely impact of the distribution on the resultant intensity evolution of Edouard. Figure 9 shows azimuth–height plots of the storm-relative radial flow averaged in the 40–60-km radial band (i.e., ~1.5–2 × RMW) for these two days. Considerable azimuthal wavenumber-1 asymmetries of radial flow are seen on both days, likely driven by a combination of storm motion and vertical shear (Shapiro 1983; Corbosiero and Molinari 2003; Zhang and Uhlhorn 2012) and the vortex tilt toward the northeast (14 September) and northwest (16 September; cf. Fig. 2). On 14 September a ~1.5-km deep layer of radial inflow is found on the north and west sides of the storm. This location of peak inflow is roughly in the forward quadrant relative to storm motion and it covers both the DSL and DSR quadrants, though there is a slight indication of stronger inflow DSR. Downwind of this feature is low-level outflow, reaching a maximum on the southeast side of the storm, at the boundary between the USL and USR quadrants. Above 2-km altitude the radial flow pattern shifts to show outflow maximized on the east and north sides (i.e., USR and DSR), and strong mid- and upper-level inflow reaching a peak on the west and south sides (DSL and USL). Above 12 km strong outflow is seen in the USL quadrant, reaching a peak magnitude at ~14 km. This feature is likely tied to the deep convection seen in Figs. 4–7. The azimuthal structure of the inflow on 16 September has similarities to that on 14 September in the lower troposphere, with peak inflow located in the forward and DSR quadrants, though the depth of the inflow is larger on 16 September. Above 8 km there is an indication of outflow on the north side consistent with a tilt toward the northwest on this day. While the radial flow pattern aloft on both days may be related to the displacement of the vortex toward the northeast at 8-km altitude (cf. Fig. 2), the overall radial flow pattern reflects quite well the azimuthal variation in radial flow created in a TC experiencing shear (e.g., Black et al. 2002; Barnes and Dolling 2013; Reasor et al. 2013; Zhang et al. 2013). Low-level inflow is strongest, and covers the most azimuthal area, in the DSR quadrant, and it is this quadrant that is the source quadrant for precipitation in the eyewall, including the deep convection on 14 September. It should be noted, however, that this result is in contrast to that shown in Sitkowski and Barnes (2009), which showed that the inflow driven by shear and storm motion, perpendicular to each other during the RI of Guillermo (1997), interacted to create an axisymmetric distribution of inflow.

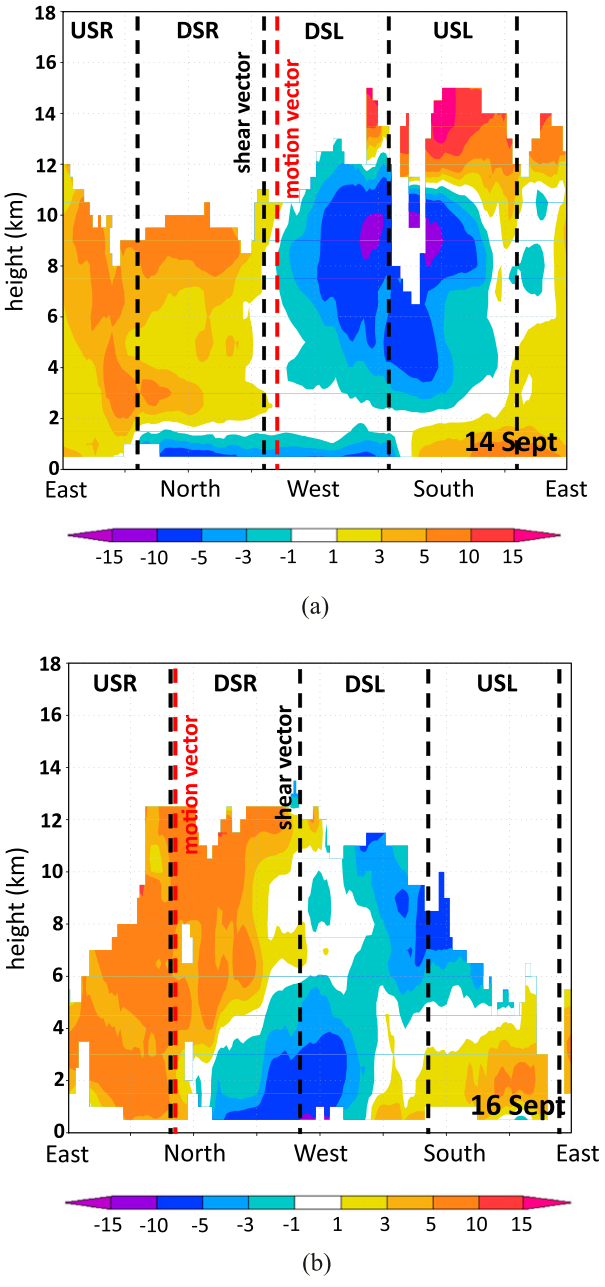

FIG. 9. (a) Azimuth–height plot of storm-relative radial flow (shaded, m s^{-1}) averaged in the 40–60-km radial band for the 14 Sep mission. Direction of storm motion (shear) labeled and indicated by red (black) dashed lines. "East," "north," etc. labels refer to Earth-relative locations. Shear-relative quadrants as indicated in Fig. 6 are labeled. (b) As in (a), but for the 16 Sep mission.

The azimuthal variation of radial flow shown in Fig. 9, and documented in the observational composite study of Reasor et al. (2013), suggests a shear-forced kinematic forcing for the observed azimuthal distribution of precipitation, including deep convection. Additional, or complementary, mechanisms for the observed azimuthal distribution of precipitation in Edouard can be identified based on the thermodynamic environment (e.g., the innermost 200 km) described in Part I. For example, Fig. 12 from Part I shows that, on 14 September, there is a distinct maximum in equivalent potential temperature θ_E inside 100-km radius to the right of the shear vector (maximized in the DSR quadrant) and a minimum in θ_E to the left of the shear vector. Such an azimuthal distribution of low-θ_E air is consistent with downdrafts from precipitation and deep convection at and inside the low-level RMW in the DSL and USL quadrants (cf. Fig. 6 from Part I; Figs. 3–8 here) cooling and drying the PBL (cf. Figs. 8, 9, 11, and 12 from Part I). With sea surface temperature (SST) values generally >27°C on 14 September (cf. Fig. 3 from Part I), the downdraft-driven low-θ_E air can be recharged by surface fluxes as it travels through the USL and USR quadrants (Molinari et al. 2013; Zhang et al. 2013). Once the air reaches the DSR quadrant, θ_E has fully recovered, as revealed by the θ_E profiles and CAPE values DSR (cf. Figs. 9 and 11 from Part I). That instability, combined with the radial inflow at the eyewall maximized DSR, are favorable conditions for the development of deep convection seen in the DSL and USL quadrants.

On 16 September, by contrast, there is a region of pronounced cooling of SST (<24°C) in the southeast part of the domain (cf. Fig. 3 from Part I), along the right-rear portion of the track, in the USL and USR quadrants. These low SST values prevent the recharge of downdraft-cooled air by surface fluxes. This results in low θ_E values in the lowest 500-m DSR and DSL, as shown in Fig. 9 from Part I. CAPE values on this day are also nearly uniformly low, as nearly all dropsondes DSR and DSL have CAPE values $<500\,\mathrm{J\,kg^{-1}}$ (cf. Fig. 11 from Part I). Despite this surface-based stabilization on 16 September, θ_E profiles still show some instability in the lower troposphere between 900 and 600 hPa (cf. Fig. 9 from Part I). Precipitation is thus observed DSL and USL, but no deep convection is present.

b. Radial distribution

Some potential mechanisms underlying the observed radial distribution are considered next. Figure 10 shows the distribution of dropsondes released from NOAA42, NOAA43, and AV6 within a 12-h window from 1200 UTC 16 September to 0000 UTC 17 September,

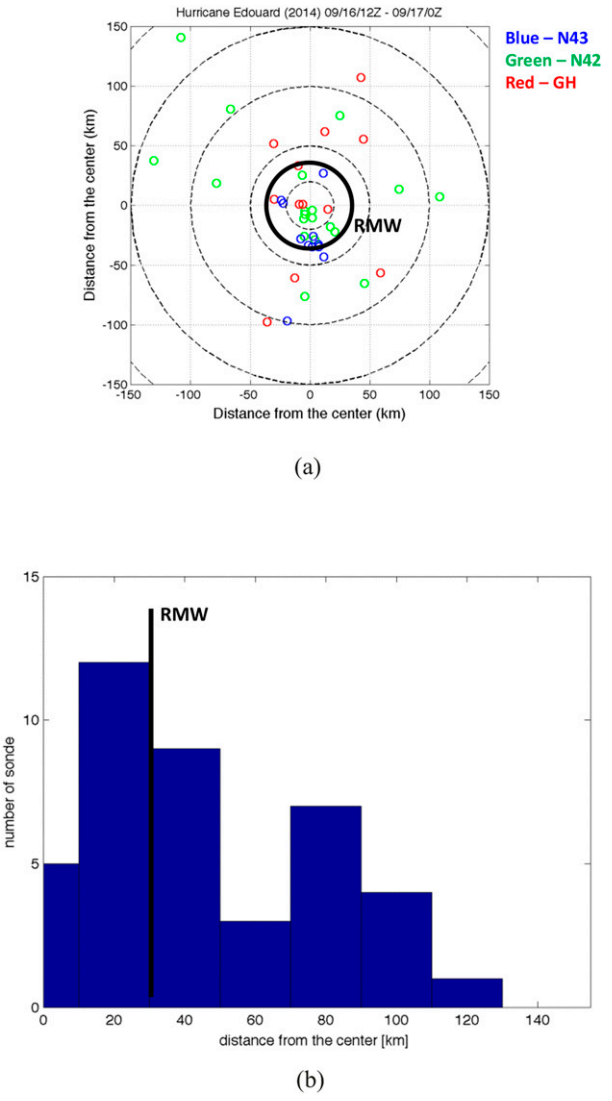

FIG. 10. (a) Distribution of dropsondes from three aircraft (NOAA42, NOAA43, and the Global Hawk) during a 12-h window centered at 1800 UTC 16 Sep. Radius of maximum wind (RMW) is indicated by thick black circle. (b) Radial distribution of dropsondes from three aircraft. Location of RMW indicated.

after Edouard had reached peak intensity and was weakening. These sondes are used to calculate PBL kinematic properties shown in Fig. 11, similar to an analysis done in Hurricane Earl (2010), which was rapidly intensifying at the time (Montgomery et al. 2014; Rogers et al. 2015). The largest number of sondes are released inside 50-km radius, at and near the RMW. However, a fairly large number of sondes are also released at outer radii (Fig. 10b). This radial distribution of sondes is comparable to that shown in the analyses of Hurricane Earl's PBL structure. Figure 11 shows radius–height profiles of azimuthally averaged radial flow, agradient wind (defined as the difference between the total wind and the

gradient flow), and divergence on 16 September. Similar to Earl (Rogers et al. 2015), inflow is maximized in the lowest few hundred meters. Both Earl and Edouard produced regions of significant supergradient flow at and inside the RMW, above 100-m altitude. Unlike Earl, however, the radial location of the peak inflow is 2–2.5 × RMW for Edouard, whereas for Earl the location was at ~1.5–2 × RMW. Furthermore, the radial location of the strongest convergence in Edouard is at ~1.5 × RMW, whereas for Earl that peak was located inside the RMW. This distribution of peak inflow and convergence outside the RMW on 16 September is likely related to the broad wind maximum and potential secondary eyewall formation on 15–16 September [not shown here but discussed in Braun et al. (2016)]. The radial location of the peak convergence outside the RMW for Edouard lends support to the idea that this PBL convergence is a key determinant of the radial location of precipitation and deep convection, and may help to explain why most of the strongest updrafts on 16 September shown in Fig. 5, while still primarily located at and inside the low-level RMW, are located radially outward from those on 14 September. Unfortunately, there was not an adequate distribution of dropsondes outside the RMW to perform a similar PBL calculation on 14 September.

Figure 12 examines the radial distribution of lower-tropospheric kinematic forcing from the airborne Doppler radar[1] within the DSR quadrant, in order to focus on the forcing mechanisms in the quadrant where convection is primarily initiated (cf. Figs. 7–9; Black et al. 2002; Braun et al. 2006; Reasor et al. 2013; DeHart et al. 2014). The top panel (Figs. 12a,b) shows a radius–height plot of radial and tangential velocity in the DSR quadrant for both 14 and 16 September. On 14 September, inflow extends inward to ~15-km radius, which is well inside the RMW in that quadrant. By contrast, on 16 September the inflow only reaches ~30-km radius, essentially stopping at the RMW. The divergence and vertical velocity fields in Figs. 12c and 12d, as expected, show convergence maximized well inside the RMW on 14 September, near ~10–15 km. This peak convergence forces an area of upward motion greater than 1.5 m s^{-1}, centered at 10-km radius. On 16 September the peak convergence has shifted radially outward, covering a

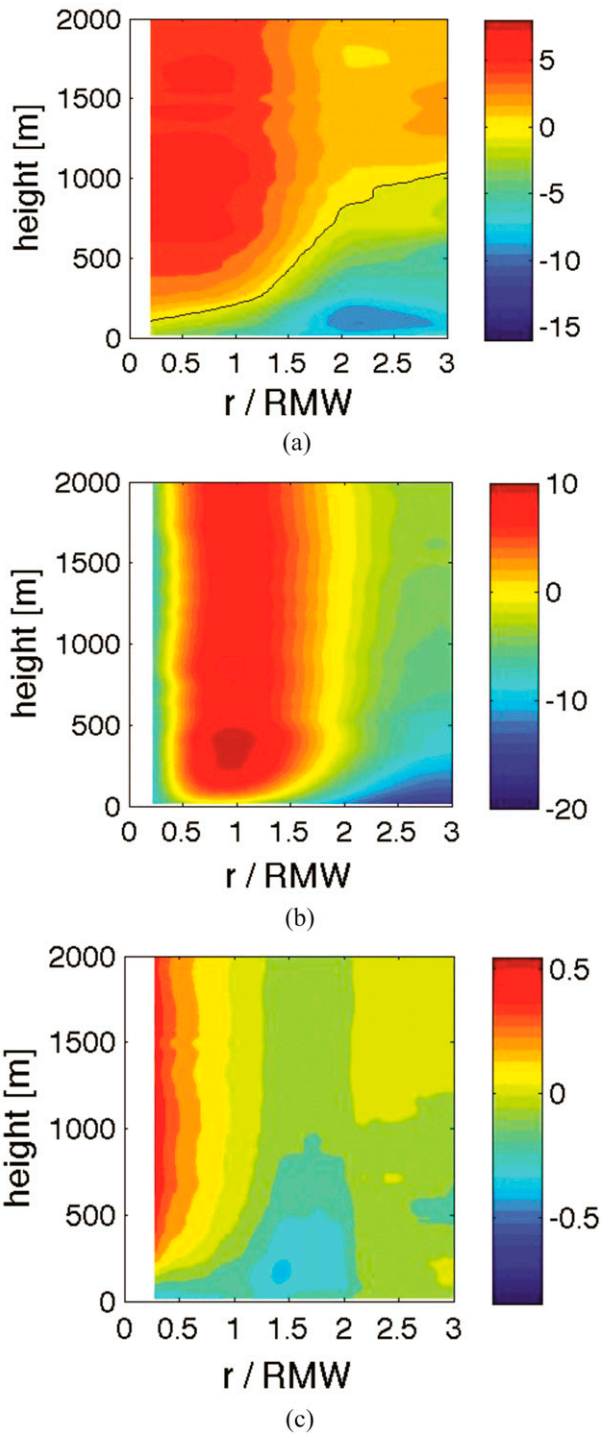

FIG. 11. (a) Radial profile of axisymmetric radial flow (shaded, m s^{-1}) in the lowest 2 km plotted as a function of normalized radius for the 12-h window centered at 1800 UTC 16 Sep as shown in Fig. 8. Black line denotes boundary between inflow and outflow. (b) As in (a), but for agradient wind (shaded, m s^{-1}). (c) As in (a), but for divergence (shaded, $\times 10^{-3}$ s^{-1}).

[1] The three-dimensional analyses from the airborne Doppler radar are limited to a lowest altitude of 500 m (Rogers et al. 2012). Thus, these analyses are unable to accurately capture the strongest inflow near 100–200-m altitude (cf. Fig. 11; Zhang et al. 2011). Nevertheless, they are capable of depicting the general characteristics of the flow in the lowest 2 km, and they do reveal distinct differences on the two days considered here, in particular in the radial structure of the fields.

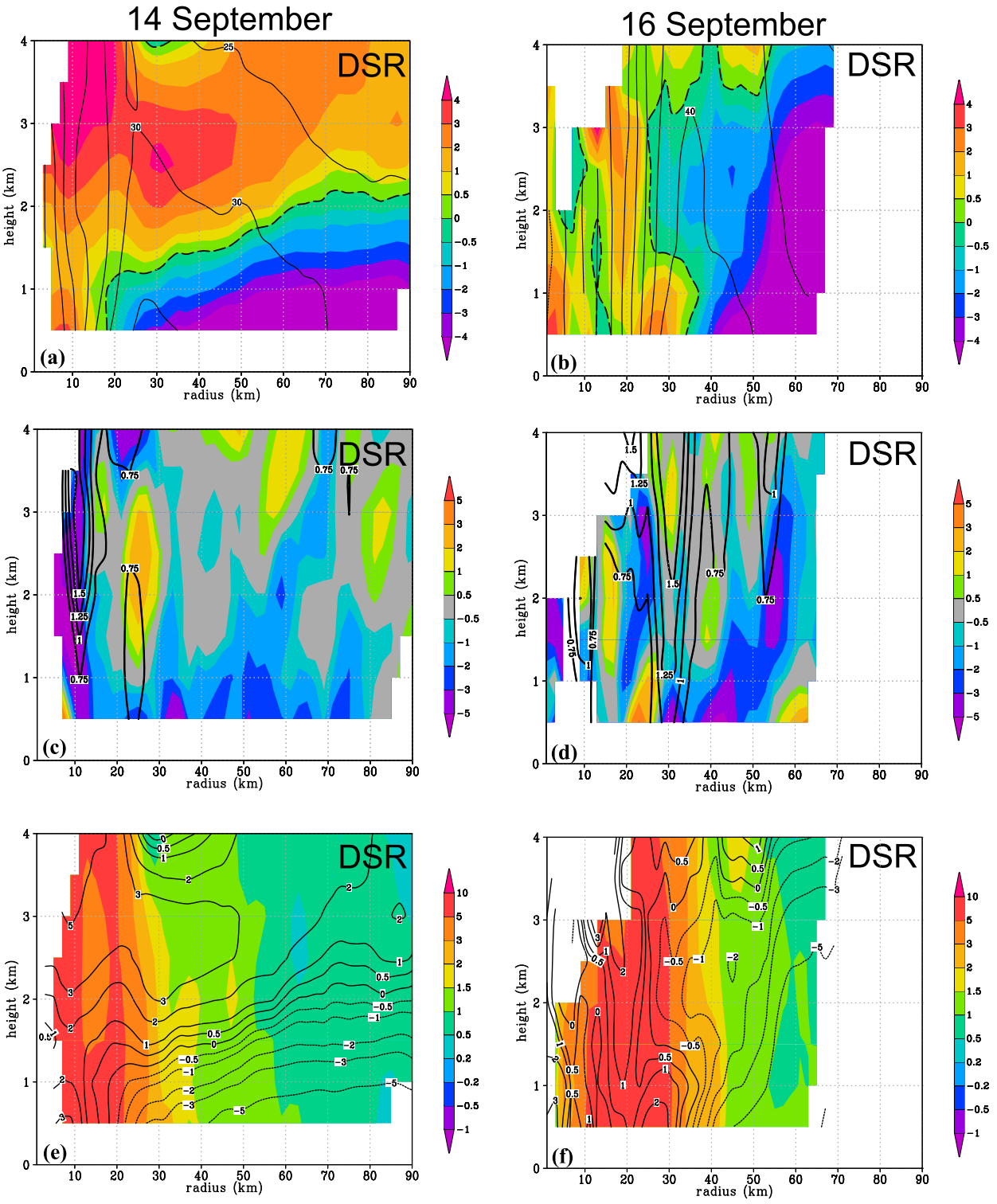

FIG. 12. (a) Radial profile of radial (shaded, m s^{-1}) and tangential wind (contour, m s^{-1}) in the 0–4-km layer averaged within the downshear-right quadrant during the 14 Sep mission. Thick dashed line denotes boundary between inflow and outflow. (b) As in (a), but for 16 Sep. (c) As in (a), but for divergence (shaded, $\times 10^{-3}$ s^{-1}) and vertical velocity (contour, 0.75, 1, 1.25, and 1.5 m s^{-1} values shown). (d) As in (c), but for 16 Sep. (e) As in (a), but for inertial stability (shaded, $\times 10^{-7}$ s^{-2}) and radial wind (contour, m s^{-1}). (f) As in (e), but for 16 Sept. In all plots, a minimum of 40% coverage within the quadrant is required before field is plotted.

radial band 30–40 km from the center. The strongest upward motion is of comparable magnitude to 14 September, but again is shifted outward to a radius of ~30 km. The inertial stability shown in Figs. 12e and 12f is higher outside the RMW (which is ~30 km on both days) on 16 September than on 14 September. In some locations outside the RMW (e.g., $r = 40$ km, $z = 3$ km), the inertial stability is nearly twice as large on 16 September than on 14 September.

The mechanism to explain the differences in the radial profile of convergence and ascent from the PBL on the two days examined here remains elusive. Differences in inertial stability could be one explanation, since from a balanced perspective inertial stability provides a greater resistance to radial displacements. A similar relationship between outer-core inertial stability and radial flow was seen in Rogers et al. (2013b, 2015). This explanation is likely valid above the frictional boundary layer (~2-km altitude), where the flow is in approximate gradient wind balance. However, within the frictional boundary layer, where gradient wind balance is not satisfied, the role of inertial stability in constraining inflow is likely invalid (e.g., Smith et al. 2015; Kilroy et al. 2016). By contrast, Miyamoto and Takemi (2015) emphasize the importance of the vortex Rossby number in determining the radial location of peak PBL convergence. They show that as storms intensify the radius of peak convergence in the PBL shifts radially outward as the Rossby number (and inertial stability) increases. This relationship may explain why the PBL convergence is farther from the center on 16 September than on 14 September. In this sense increased inertial stability in the PBL could serve as a self-limiting mechanism, essentially moving the radial location of peak convergence to a larger distance from the center. Another potential mechanism modulating the radial location of PBL convergence is the cooling in the right-rear quadrant of Edouard on 16 September. Lee and Chen (2014) showed that a stable boundary layer in this quadrant can lead to enhanced inflow into the inner core. However, the convergence profiles DSR (Figs. 12a,b) show that the convergence is actually displaced radially outward on 16 September, in contrast to that suggested in Lee and Chen (2014). The linkage between the TC PBL and convection is an area of active research, and the results shown here provide an important observational benchmark for these studies.

c. *Impact of spatial and temporal distributions on intensity evolution*

The quadrant-averaged distribution of vertical velocity and inertial stability are shown in the DSL and USL quadrants for the merged analyses for 14 and 16 September (Fig. 13). These quadrants are located downwind of where convection is primarily initiated. On 14 September, an area of upward motion is seen at 4-km altitude at a radius of 15 km in the DSL quadrant (Fig. 13b). Farther aloft this upward motion exceeds 2.5 m s^{-1} (in a quadrant-averaged sense) inside the local RMW at that altitude. This strong upward motion also coincides with high inertial stability in the inner core. Continuing downwind into the USL quadrant (Fig. 13a), the strong upward motion continues above 10-km altitude, however, there is now also a broad region of subsidence below. Such a distribution of upward motion in the quadrant average is consistent with the presence of deep convection in this quadrant (cf. Figs. 4–7). Additionally, the strong upward motion above 10-km USL inside the RMW is coincident with high inertial stability, similar to the DSL quadrant. On 16 September, there is an area of upward motion inside the local RMW in the DSL quadrant. However, this upward motion is weaker than on 14 September, and there is less overlap with the region of high inertial stability in this quadrant. Looking at the USL quadrant on 16 September, a small area of weak upward motion is again consistent with the lack of deep convection here (cf. Figs. 4–7).

The intensification of Edouard on 14 September may be tied to the fact that diabatic heating associated with the strong upward motion is collocated with high inertial stability inside the RMW in the DSL and USL quadrants. Such a distribution of heating is more efficient at being converted to kinetic energy of the rotational flow (Schubert and Hack 1982; Shapiro and Willoughby 1982; Nolan et al. 2007; Vigh and Schubert 2009; Pendergrass and Willoughby 2009). With limited overlap between the upward motion and high inertial stability in both of these quadrants on 16 September, there is little tendency to spin up the vortex. An alternate interpretation of the importance of the radial location of diabatic heating and vortex spinup is offered in Smith et al. (2015), Kilroy et al. (2016), and Smith and Montgomery (2016). They make the point that, rather than making arguments regarding heating efficiency, the role of deep convection can be more succinctly understood simply by considering that angular momentum surfaces are advected inward (outward) in the frictional boundary layer when deep convection occurs inside (outside) the RMW. The role of the PBL in TC intensification in the context of angular momentum advection is more direct than the efficiency arguments, which may or may not intensify the vortex depending on the location of the deep convection relative to the high inertial stability region of the inner core. Regardless of which role the PBL plays in intensification (i.e., a direct role involving advection of angular momentum surfaces in the frictional boundary layer versus an indirect role involving forcing of deep convection via

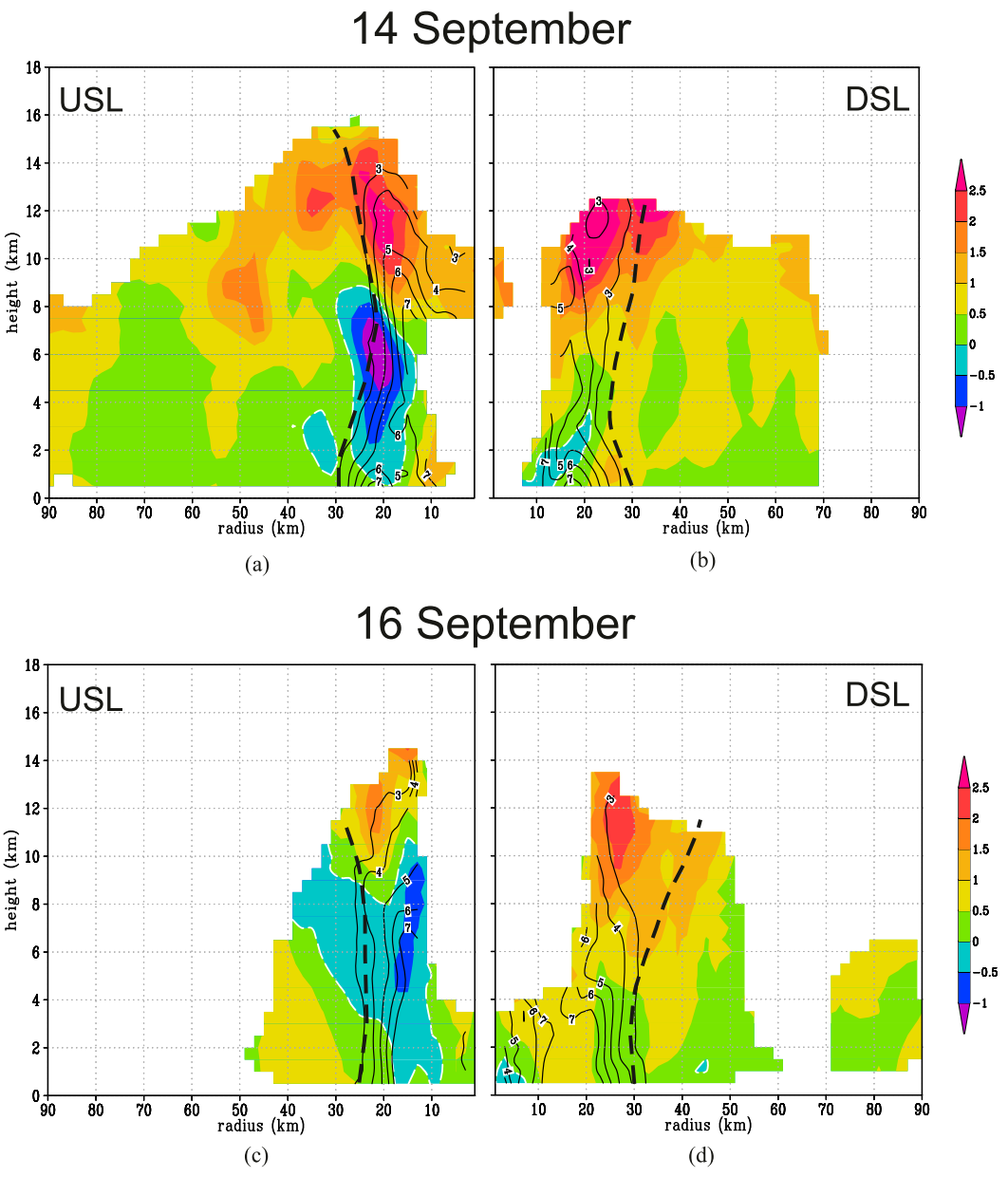

FIG. 13. (a) Radial profile of vertical velocity (shaded, m s^{-1}) and inertial stability (contour, $\times 10^{-7}$ s^{-2}) averaged within the upshear-left quadrant during the 14 Sep mission. Thick black dashed line denotes quadrant-averaged RMW, and thin white dashed line denotes zero contour for vertical velocity. (b) As in (a), but for downshear-left quadrant. (c) As in (a), but for 16 Sep. (d) As in (b), but for 16 Sep. In all plots, a minimum of 40% coverage is required before field is plotted. Note inverted x axes in (a) and (c).

PBL convergence), both mechanisms require a favorable location of deep convection inside the RMW.

5. Discussion and conclusions

a. Support for three hypotheses

The extensive datasets analyzed in this two-part study provide a unique opportunity to describe the thermodynamic and kinematic structure of the inner core and near environment of Edouard as it underwent several different stages of intensity evolution. In recent years, the literature on intensity change has increasingly pointed to the potential importance of symmetry of latent heating, the azimuthal location of deep convection with respect to environmental shear, and the radial location of deep convection with respect to the radius of

maximum wind. We believe that the results from Edouard are helpful in articulating and lending support for three hypotheses that may be helpful in understanding intensity change.

A common aspect of the discussion in this two-part study pertains to the role of symmetry in Edouard's intensification. From these observations, symmetry applies to both the thermodynamic and precipitation structure, spanning a broad domain within and around the storm. Precipitation as indicated by the passive microwave satellite data showed a distinct tendency to transition from a less symmetric state during the slowly intensifying stage on 12 September, to a more symmetric state during the near-rapid intensification on 14 September, to a period of maximum symmetry once the storm had reached peak intensity on 16 September (cf. Figs. 6 and 8 in Part I). A similar evolution in symmetry was seen in the profiles of relative humidity and θ_E between 12–16 September (cf. Figs. 9 and 10 in Part I). The notion of symmetry can be defined relative to the shear vector, which was of moderate intensity from the southwest on 12 September and from the southeast on 14–16 September. Within this framework, changes in symmetry are most closely tied to changes in the upshear quadrants on these days; that is, the most significant changes in humidity, θ_E, precipitation (broadly speaking), and deep convection (specifically) were seen upshear. These observations lead to the first hypothesis to arise from this work:

Hypothesis 1:

- *Increased azimuthal coverage of deep convection, particularly when present in the upshear quadrants, contributes to a greater symmetry of diabatic heating and is a favorable configuration for vortex spinup.*

Several possible mechanisms, many of which were shown here and in Part I, can modulate the distribution of deep convection upshear. Entrainment of dry air into the inner core can impact the strength of the convection, either by forcing downdrafts through evaporation in the lower troposphere or reducing updraft strength through detrainment in the middle/upper troposphere. The impact of this weakening of the convection upshear on the TC intensity is similar to that described in Tang and Emanuel (2010). The source of the dry air upshear in the case of Edouard did not appear to be from the environment, as the local environment did not have any pronounced regions of dry air. Rather, dry air appeared to be driven by subsidence, especially during the first few days Edouard was sampled (cf. Figs. 14 and 15 in Part I). Differences in the azimuthal distributions of CAPE can also modulate the precipitation distribution. As shown in Part I (cf. Figs. 10 and 12 in Part I), CAPE, as well as vertical profiles of θ_E, showed that the most unstable quadrant was the downshear right quadrant on 14 September.

While humidity distributions can impact stability through entrainment processes, another key element is the lower boundary condition. In the case of Edouard, the presence of warm water around the storm on 14 September (cf. Fig. 3 in Part I) likely played a significant role in allowing the PBL to recover from convection downshear left and upshear left, resulting in an unstable environment downshear right (Molinari et al. 2013; Zhang et al. 2013). When combined with the maximum radial inflow in that quadrant (cf. Fig. 9 here), this provided a favorable environment for the initiation and maintenance of deep convection downwind (i.e., downshear left and upshear left). The sea surface cooling seen two days later, partially induced by Edouard itself, likewise likely played a role in limiting the destabilization downshear right (cf. Figs. 10 and 12 in Part I), contributing to the lack of deep convection seen on that day (cf. Figs. 4–7 here) and subsequent lack of intensification, in a manner similar to that discussed in Riemer et al. (2010).

Other factors can impact the distribution of deep convection upshear. The development of the upper-level warm core played a role in constraining CAPE, especially as the warm core developed later in the storm's life cycle (cf. Fig. 11 in Part I). Tilt of the vortex can drive asymmetries in the low-level convergence at the eyewall (e.g., Reasor et al. 2009; Reasor and Eastin 2012; Reasor et al. 2013). Tilt has also been shown to drive low-level convergence outside the eyewall on the downshear side, leading to downdraft cooling at large radii and weakening the precipitation at the eyewall (e.g., Riemer et al. 2010). Displacement of the circulation center thus can clearly hinder intensification. While Edouard did show some tilt (at least on 14–16 September; cf. Fig. 2 here), this is not considered to play a significant role in modulating the intensity change. Finally, environmental helicity (Onderlinde and Nolan 2014, 2016) has been shown to be a parameter that can control the longevity and robustness of convection in tropical cyclones, particularly upshear. Onderlinde and Nolan (2016) related PBL recovery to storm-relative helicity, showing that the boundary layer downwind of deep convection recovered more quickly for storms encountering positive helicity. This was not investigated here, but future work should include a consideration of helicity in modulating the azimuthal distribution of convection.

The radial distribution of deep convection and its relationship with the intensity evolution of Edouard (cf. Fig. 13 here) is consistent with previous studies showing the importance of diabatic heating occurring in the

high-inertial stability region inside the RMW (e.g., Shapiro and Willoughby 1982; Schubert and Hack 1982; Nolan et al. 2007; Vigh and Schubert 2009; Pendergrass and Willoughby 2009; Rogers et al. 2013b, 2015; Susca-Lopata et al. 2015). The radial location of peak PBL convergence while Edouard was weakening on 16 September (cf. Figs. 11 and 12 here), and its comparison with the radial location in Hurricane Earl (2010) when it was intensifying (cf. Rogers et al. 2015), supports the idea that PBL convergence is a key forcing mechanism governing the radial distribution of deep convection and the subsequent vortex response. Differences in the PBL convergence between the two days, and hence the forcing for deep convection, were evident in the downshear-right quadrant (cf. Fig. 12 here). Differences in the location of strong updrafts relative to the inertial stability were clear in the downshear-left and upshear-left quadrants (cf. Fig. 13 here). Such an analysis suggests that it is necessary to focus on forcing mechanisms and the environment of the deep convection in specific, shear-relative quadrants. This leads to the second hypothesis:

Hypothesis 2:

- *The radial location for the forcing of deep convection around the TC is largely determined by the conditions in the azimuthal location where the convection is primarily initiated (e.g., the DSR quadrant in sheared storms), while the environment of the deep convection must be examined downwind (e.g., DSL and USL).*

To the extent that TC intensification is driven by deep convection, a useful framework for interpreting its role in TC intensification is to consider the spatial and temporal structure and evolution of both the forcing mechanisms and the local environment of the convection. Kinematic properties such as PBL convergence and outer-core inertial stability, and thermodynamic properties such as low-level destabilization through surface fluxes, provide and modulate the forcing mechanism for convection. Thermodynamic fields like relative humidity and the upper-level warm core, as well as kinematic fields such as inner-core inertial stability and angular momentum distributions, provide the local environment that supports (or suppresses) convection and governs the response of the vortex to the diabatic heating from the convection. Both of these factors (i.e., the forcing mechanisms and the local environment of convection) can exhibit significant asymmetries, especially in the presence of vertical shear. However, whether or not the TC will intensify is dependent on the extent to which the convection is distributed symmetrically and located primarily inside the RMW. This leads to the third and final hypothesis:

Hypothesis 3:

- *The forcing and local environment of deep convection are key in determining its role in TC intensification; governing whether the convection is symmetrically distributed and primarily inside the RMW.*

The structure of both the forcing and the local environment can exhibit distinct asymmetries, but the likelihood of TC intensification is enhanced if the convection is symmetrically distributed and located primarily inside the RMW. This is particularly important when a feature that promotes azimuthal asymmetries, such as vertical shear, is present. In the case of vertical shear, the forcing for deep convection is confined to the DSR and DSL quadrants. If the convection remains there and does not propagate upshear, then intensification is less likely to occur. Conversely, if deep convection does propagate upshear, as was seen here on 14 September, then intensification is more likely. The key is to identify what determines whether the deep convection can persist and propagate upshear.

These ideas can also be interpreted in a similar way for symmetric storms. For example, in cases where the shear is weak and storm translation is relatively small, or their directions are perpendicular to each other in a way that they constructively interfere with each other as in Sitkowski and Barnes (2009), then the forcing and the environment of the convection will be relatively symmetric. In those situations the TC will be even more likely to intensify.

b. Future work

Despite the uniqueness of the datasets described here, there are areas for further inquiry, as well as a need for better datasets. For example, it is still not clear from this study whether it is the distribution of deep or shallow/moderate convection that is more important for intensification, something that is the subject of ongoing research (e.g., Tao and Jiang 2015). The results of this study seem to suggest that they may play an equally important role, since both experience an increase in occurrence upshear during intensification. One question to consider is whether the forcing mechanisms for deep convection discussed here (e.g., PBL convergence, outer-core inertial stability, etc.) also play a role in governing both the radial and azimuthal distribution of shallow/moderate convection. Another question to consider is other modes of precipitation, such as stratiform precipitation. For example, the vertical velocity

USL on 14 September, shown in Figs. 7 and 13, indicates a clear region of deep-layer subsidence below 8 km, overlain by updrafts above 10 km. In the environment of a typical midlatitude or tropical convective system, that is generally an indication of stratiform precipitation (Houze 1977; Zipser 1977; Gamache and Houze 1982; Johnson 1984; Mapes and Houze 1995). However, in the eyewall region of a TC this is less certain, since it could reflect the azimuthal trajectory of strong updrafts initiated downshear right. As a result, the mechanisms responsible for the convective to stratiform transition in this unique environment should be studied further. For example, to what extent is the subsidence USL reflective of stratiform precipitation processes as opposed to being generated by the interaction of shear with the vortex?

Additional datasets are needed to answer these questions. Combined satellite and aircraft datasets, nearly coincident in space and concurrent in time, can provide a broader context for the vortex and precipitation structures, and their relationship with intensity change, vertical shear, and storm motion. Numerical models can also help to address these questions. Time continuity from the models can provide information on the evolution of precipitation, rather than the snapshots available from intermittent aircraft or satellite sampling. Trajectory calculations can be made to identify the source regions of the precipitation and better characterize the precipitation as deep convection, shallow/moderate convection, stratiform, etc. One important question to consider when using numerical models is how well the models represent the structures and processes (e.g., PBL, microphysics, air–sea interaction) that are important in intensity change. To perform these evaluations new datasets are also needed. In particular, PBL measurements from dropsondes and low-level unmanned systems (Cione et al. 2016, manuscript submitted to *J. Atmos. Oceanic Technol.*) are needed, as are precipitation and microphysics measurements from airborne and ground-based radar and satellites. Polarimetric radar, whether ground-based (Melnikov et al. 2011) or airborne (Bluestein et al. 2014), is another promising dataset for microphysical evaluations. Ocean measurements from airborne expendables and dropsondes capable of measuring the sea surface temperature along with air temperature can provide measurements at the air–sea interface. Finally, aircraft missions that specifically target sheared storms are needed to sample these fields and augment the existing database of measurements.

The analysis shown here documents the inner-core and environmental conditions associated with a TC that nearly underwent RI. While identifying such conditions is a worthwhile endeavor, rapidly intensifying TCs simply represent the tail end of a near-normal distribution of intensity changes (Kowch and Emanuel 2015), suggesting that there is no special set of physical processes that govern RI. Stated another way, given a favorable environmental and inner-core structure, all TCs will intensify, unless they are hindered by vertical shear, dry air, and/or an unfavorable azimuthal and radial distribution of precipitation. The challenge is to identify where and when the negative influences (both environmental and vortex scale) will be significant enough to hinder intensification. This research attempts this, but more research, in a variety of cases with different environments, inner-core structures, and intensity evolutions, are required to adequately test the hypotheses discussed here.

Acknowledgments. This research is supported by NASA HS3 Grants NNX11AB59G, NNG11HG00I, and NNX15AN30H and NASA Hurricane Science Research Project (HSRP) Grant NNX10AG34G, under the leadership and direction of Dr. Ramesh Kakar; the NOAA Joint Hurricane Testbed (JHT) Grants NA13OAR4590191 and NA15OAR4590199, under the direction of Dr. Chris Landsea (NHC); the NOAA Hurricane Forecast Improvement Project (HFIP) Grant NA14NWS4680028; the National Science Foundation Grant AGS1249732; and NOAA base funds. The airborne datasets would not be possible without the efforts of the NASA HS3 and NOAA IFEX teams, as well as personnel at the NOAA Aircraft Operations Center. HS3 dropsonde data were quality controlled by staff at NCAR EOL, with support from the National Science Foundation, and NOAA/AOML/HRD. Comments from Drs. Paul Reasor and Hua Chen of NOAA/AOML/HRD and three anonymous reviewers helped to improve the manuscript. The authors wish to thank the World Wide Lightning Location Network (http://wwlln.net), a collaboration among over 50 universities and institutions, for providing the lightning location data used in this paper.

REFERENCES

Alvey, G. R., III, J. Zawislak, and E. Zipser, 2015: Precipitation properties observed during tropical cyclone intensity change. *Mon. Wea. Rev.*, **143**, 4476–4492, doi:10.1175/MWR-D-15-0065.1.

Barnes, G. M., and K. P. Dolling, 2013: The inflow to Tropical Cyclone Humberto (2001) as viewed with azimuth–height surfaces over three days. *Mon. Wea. Rev.*, **141**, 1324–1336, doi:10.1175/MWR-D-11-00348.1.

Bender, M. A., 1997: The effect of relative flow on the asymmetric structure in the interior of hurricanes. *J. Atmos. Sci.*, **54**, 703–724, doi:10.1175/1520-0469(1997)054<0703:TEORFO>2.0.CO;2.

Black, M. L., J. F. Gamache, F. D. Marks, C. E. Samsury, and H. E. Willoughby, 2002: Eastern Pacific Hurricanes Jimena of 1991 and Olivia of 1994: The effect of vertical shear on structure and intensity. *Mon. Wea. Rev.*, **130**, 2291–2312, doi:10.1175/1520-0493(2002)130<2291:EPHJOA>2.0.CO;2.

Bluestein, H. B., and Coauthors, 2014: Radar in atmospheric sciences and related research: Current systems, emerging technology, and future needs. *Bull. Amer. Meteor. Soc.*, **95**, 1850–1861, doi:10.1175/BAMS-D-13-00079.1.

Braun, S. A., M. T. Montgomery, and Z. Pu, 2006: High-resolution simulation of Hurricane Bonnie (1998). Part I: The organization of eyewall vertical motion. *J. Atmos. Sci.*, **63**, 19–42, doi:10.1175/JAS3598.1.

——, P. A. Newman, and G. M. Heymsfield, 2016: NASA's Hurricane and Severe Storm Sentinel (HS3) Investigation. *Bull. Amer. Meteor. Soc.*, doi:10.1175/BAMS-D-15-00186.1, in press.

Chen, H., and D. L. Zhang, 2013: On the rapid intensification of Hurricane Wilma (2005). Part II: Convective bursts and the upper-level warm core. *J. Atmos. Sci.*, **70**, 146–162, doi:10.1175/JAS-D-12-062.1.

——, and S. G. Gopalakrishnan, 2015: A study on the asymmetric rapid intensification of Hurricane Earl (2010) using the HWRF system. *J. Atmos. Sci.*, **72**, 531–550, doi:10.1175/JAS-D-14-0097.1.

Corbosiero, K. L., and J. Molinari, 2003: The relationship between storm motion, vertical wind shear, and convective asymmetries in tropical cyclones. *J. Atmos. Sci.*, **60**, 366–376, doi:10.1175/1520-0469(2003)060<0366:TRBSMV>2.0.CO;2.

Cram, T. A., J. Persing, M. T. Montgomery, and S. A. Braun, 2007: A Lagrangian trajectory view on transport and mixing processes between the eye, eyewall, and environment using a high-resolution simulation of Hurricane Bonnie (1998). *J. Atmos. Sci.*, **64**, 1835–1856, doi:10.1175/JAS3921.1.

DeHart, J. C., R. A. Houze Jr., and R. F. Rogers, 2014: Quadrant distribution of tropical cyclone inner-core kinematics in relation to environmental shear. *J. Atmos. Sci.*, **71**, 2713–2732, doi:10.1175/JAS-D-13-0298.1.

DeMaria, M., 1996: The effect of vertical shear on tropical cyclone intensity change. *J. Atmos. Sci.*, **53**, 2076–2088, doi:10.1175/1520-0469(1996)053<2076:TEOVSO>2.0.CO;2.

Dolling, K., and G. M. Barnes, 2014: The evolution of Hurricane Humberto (2001). *J. Atmos. Sci.*, **71**, 1276–1291, doi:10.1175/JAS-D-13-0164.1.

Emanuel, K., C. DesAutels, C. Holloway, and R. Korty, 2004: Environmental control of tropical cyclone intensity. *J. Atmos. Sci.*, **61**, 843–858, doi:10.1175/1520-0469(2004)061<0843:ECOTCI>2.0.CO;2.

Frank, W. M., and E. A. Ritchie, 2001: Effects of vertical wind shear on the intensity and structure of numerically simulated hurricanes. *Mon. Wea. Rev.*, **129**, 2249–2269, doi:10.1175/1520-0493(2001)129<2249:EOVWSO>2.0.CO;2.

Gamache, J. F., 1997: Evaluation of a fully three-dimensional variational Doppler analysis technique. Preprints, *28th Conf. on Radar Meteorology*, Austin, TX, Amer. Meteor. Soc., 422–423.

——, and R. A. Houze Jr., 1982: Mesoscale air motions associated with a tropical squall line. *Mon. Wea. Rev.*, **110**, 118–135, doi:10.1175/1520-0493(1982)110<0118:MAMAWA>2.0.CO;2.

Guimond, S. R., G. M. Heymsfield, and F. J. Turk, 2010: Multiscale observations of Hurricane Dennis (2005): The effects of hot towers on rapid intensification. *J. Atmos. Sci.*, **67**, 633–654, doi:10.1175/2009JAS3119.1.

Halverson, J. B., J. Simpson, G. Heymsfield, H. Pierce, T. Hock, and L. Ritchie, 2006: Warm core structure of Hurricane Erin diagnosed from high altitude dropsondes during CAMEX-4. *J. Atmos. Sci.*, **63**, 309–324, doi:10.1175/JAS3596.1.

Hazelton, A. T., R. F. Rogers, and R. E. Hart, 2015: Shear-relative asymmetries in tropical cyclone eyewall slope. *Mon. Wea. Rev.*, **143**, 883–903, doi:10.1175/MWR-D-14-00122.1.

Hendricks, E. A., M. T. Montgomery, and C. A. Davis, 2004: The role of "vortical" hot towers in the formation of Tropical Cyclone Diana (1984). *J. Atmos. Sci.*, **61**, 1209–1232, doi:10.1175/1520-0469(2004)061<1209:TROVHT>2.0.CO;2.

Houze, R. A., Jr., 1977: Structure and dynamics of a tropical squall-line system. *Mon. Wea. Rev.*, **105**, 1540–1567, doi:10.1175/1520-0493(1977)105<1540:SADOAT>2.0.CO;2.

Jiang, H., 2012: The relationship between tropical cyclone intensity change and the strength of inner-core convection. *Mon. Wea. Rev.*, **140**, 1164–1176, doi:10.1175/MWR-D-11-00134.1.

Johnson, R. H., 1984: Partitioning tropical heat and moisture budgets into cumulus and mesoscale components: Implications for cumulus parameterization. *Mon. Wea. Rev.*, **112**, 1590–1601, doi:10.1175/1520-0493(1984)112<1590:PTHAMB>2.0.CO;2.

Jones, S. C., 1995: The evolution of vortices in vertical shear. I: Initially barotropic vortices. *Quart. J. Roy. Meteor. Soc.*, **121**, 821–851, doi:10.1002/qj.49712152406.

Kelley, O. A., J. Stout, and J. B. Halverson, 2004: Tall precipitation cells in tropical cyclone eyewalls are associated with tropical cyclone intensification. *Geophys. Res. Lett.*, **31**, L24112, doi:10.1029/2004GL021616.

Kepert, J. D., 2001: The dynamics of boundary layer jets within the tropical cyclone core. Part I: Linear theory. *J. Atmos. Sci.*, **58**, 2469–2484, doi:10.1175/1520-0469(2001)058<2469:TDOBLJ>2.0.CO;2.

——, and Y. Wang, 2001: The dynamics of boundary layer jets within the tropical cyclone core. Part II: Nonlinear enhancement. *J. Atmos. Sci.*, **58**, 2485–2501, doi:10.1175/1520-0469(2001)058<2485:TDOBLJ>2.0.CO;2.

Kieper, M. E., and H. Jiang, 2012: Predicting tropical cyclone rapid intensification using the 37 GHz ring pattern identified from passive microwave measurements. *Geophys. Res. Lett.*, **39**, L13804, doi:10.1029/2012GL052115.

Kilroy, G., R. K. Smith, and M. T. Montgomery, 2016: Why do model tropical cyclones grow progressively in size and decay in intensity after reaching maturity? *J. Atmos. Sci.*, **73**, 487–503, doi:10.1175/JAS-D-15-0157.1.

Kowch, R., and K. Emanuel, 2015: Are special processes at work in the rapid intensification of tropical cyclones? *Mon. Wea. Rev.*, **143**, 878–882, doi:10.1175/MWR-D-14-00360.1.

Lay, E. H., R. H. Holzworth, C. J. Rodger, J. N. Thomas, O. Pinto Jr., and R. L. Dowden, 2004: WWLL global lightning detection system: Regional validation study in Brazil. *Geophys. Res. Lett.*, **31**, L03102, doi:10.1029/2003GL018882.

Lee, C.-Y., and S. S. Chen, 2014: Stable boundary layer and its impact on tropical cyclone structure in a coupled atmosphere–ocean model. *Mon. Wea. Rev.*, **142**, 1927–1944, doi:10.1175/MWR-D-13-00122.1.

Mapes, B. E., and R. A. Houze Jr., 1995: Diabatic divergence profiles in western Pacific mesoscale convective systems. *J. Atmos. Sci.*, **52**, 1807–1828, doi:10.1175/1520-0469(1995)052<1807:DDPIWP>2.0.CO;2.

Melnikov, V. M., D. S. Zrnić, R. J. Doviak, P. B. Chilson, D. B. Mechem, and Y. L. Kogan, 2011: Prospects of the WSR-88D radar for cloud studies. *J. Appl. Meteor. Climatol.*, **50**, 859–872, doi:10.1175/2010JAMC2303.1.

Miyamoto, Y., and T. Takemi, 2015: A triggering mechanism for rapid intensification of tropical cyclones. *J. Atmos. Sci.*, **72**, 2666–2681, doi:10.1175/JAS-D-14-0193.1.

Molinari, J., and D. Vollaro, 2010: Rapid intensification of a sheared tropical storm. *Mon. Wea. Rev.*, **138**, 3869–3885, doi:10.1175/2010MWR3378.1.

——, ——, and K. L. Corbosiero, 2004: Tropical cyclone formation in a sheared environment: A case study. *J. Atmos. Sci.*, **61**, 2493–2509, doi:10.1175/JAS3291.1.

——, P. Dodge, D. Vollaro, K. L. Corbosiero, and F. Marks, 2006: Mesoscale aspects of the downshear reformation of a tropical cyclone. *J. Atmos. Sci.*, **63**, 341–354, doi:10.1175/JAS3591.1.

——, J. Frank, and D. Vollaro, 2013: Convective bursts, downdraft cooling, and boundary layer recovery in a sheared tropical storm. *Mon. Wea. Rev.*, **141**, 1048–1060, doi:10.1175/MWR-D-12-00135.1.

Montgomery, M. T., M. Nicholls, T. Cram, and A. Saunders, 2006: A ''vortical'' hot tower route to tropical cyclogenesis. *J. Atmos. Sci.*, **63**, 355–386, doi:10.1175/JAS3604.1.

——, J. A. Zhang, and R. K. Smith, 2014: An analysis of the observed low-level structure of rapidly intensifying and mature Hurricane Earl (2010). *Quart. J. Roy. Meteor. Soc.*, **140**, 2132–2146, doi:10.1002/qj.2283.

Nguyen, L. T., and J. Molinari, 2012: Rapid intensification of a sheared, fast-moving hurricane over the Gulf Stream. *Mon. Wea. Rev.*, **140**, 3361–3378, doi:10.1175/MWR-D-11-00293.1.

——, and ——, 2015: Simulation of the downshear reformation of a tropical cyclone. *J. Atmos. Sci.*, **72**, 4529–4551, doi:10.1175/JAS-D-15-0036.1.

Nolan, D. S., Y. Moon, and D. P. Stern, 2007: Tropical cyclone intensification from asymmetric convection: Energetics and efficiency. *J. Atmos. Sci.*, **64**, 3377–3405, doi:10.1175/JAS3988.1.

Onderlinde, M. J., and D. S. Nolan, 2014: Environmental helicity and its effects on development and intensification of tropical cyclones. *J. Atmos. Sci.*, **71**, 4308–4320, doi:10.1175/JAS-D-14-0085.1.

——, and ——, 2016: Tropical cyclone–relative environmental helicity and the pathways to intensification in shear. *J. Atmos. Sci.*, **73**, 869–890, doi:10.1175/JAS-D-15-0261.1.

Pendergrass, A. G., and H. E. Willoughby, 2009: Diabatically induced secondary flows in tropical cyclones. Part I: Quasi-steady forcing. *Mon. Wea. Rev.*, **137**, 805–821, doi:10.1175/2008MWR2657.1.

Reasor, P. D., and M. D. Eastin, 2012: Rapidly intensifying Hurricane Guillermo (1997). Part II: Resilience in shear. *Mon. Wea. Rev.*, **140**, 425–444, doi:10.1175/MWR-D-11-00080.1.

——, ——, and J. F. Gamache, 2009: Rapidly intensifying Hurricane Guillermo (1997). Part I: Low-wavenumber structure and evolution. *Mon. Wea. Rev.*, **137**, 603–631, doi:10.1175/2008MWR2487.1.

——, R. F. Rogers, and S. Lorsolo, 2013: Environmental flow impacts on tropical cyclone structure diagnosed from airborne Doppler radar composites. *Mon. Wea. Rev.*, **141**, 2949–2969, doi:10.1175/MWR-D-12-00334.1.

Riehl, H., and J. S. Malkus, 1961: Some aspects of Hurricane Daisy. *Tellus*, **13**, 181–213, doi:10.1111/j.2153-3490.1961.tb00077.x.

Riemer, M., M. T. Montgomery, and M. E. Nicholls, 2010: A new paradigm for intensity modification of tropical cyclones: Thermodynamic impact of vertical wind shear on the inflow layer. *Atmos. Chem. Phys.*, **10**, 3163–3188, doi:10.5194/acp-10-3163-2010.

Rogers, R., 2010: Convective-scale structure and evolution during a high-resolution simulation of tropical cyclone rapid intensification. *J. Atmos. Sci.*, **67**, 44–70, doi:10.1175/2009JAS3122.1.

——, S. S. Chen, J. E. Tenerelli, and H. E. Willoughby, 2003: A numerical study of the impact of vertical shear on the distribution of rainfall in Hurricane Bonnie (1998). *Mon. Wea. Rev.*, **131**, 1577–1599, doi:10.1175//2546.1.

——, S. Lorsolo, P. D. Reasor, J. Gamache, and F. D. Marks Jr., 2012: Multiscale analysis of tropical cyclone kinematic structure from airborne Doppler radar composites. *Mon. Wea. Rev.*, **140**, 77–99, doi:10.1175/MWR-D-10-05075.1.

——, and Coauthors, 2013a: NOAA's Hurricane Intensity Forecasting Experiment: A progress report. *Bull. Amer. Meteor. Soc.*, **94**, 859–882, doi:10.1175/BAMS-D-12-00089.1.

——, P. D. Reasor, and S. Lorsolo, 2013b: Airborne Doppler observations of the inner-core structural differences between intensifying and steady-state tropical cyclones. *Mon. Wea. Rev.*, **141**, 2970–2991, doi:10.1175/MWR-D-12-00357.1.

——, ——, and J. A. Zhang, 2015: Multiscale structure and evolution of Hurricane Earl (2010) during rapid intensification. *Mon. Wea. Rev.*, **143**, 536–562, doi:10.1175/MWR-D-14-00175.1.

Schubert, W. H., and J. J. Hack, 1982: Inertial stability and tropical cyclone development. *J. Atmos. Sci.*, **39**, 1687–1697, doi:10.1175/1520-0469(1982)039<1687:ISATCD>2.0.CO;2.

Shapiro, L. J., 1983: Asymmetric boundary layer flow under a translating hurricane. *J. Atmos. Sci.*, **40**, 1984–1998, doi:10.1175/1520-0469(1983)040<1984:TABLFU>2.0.CO;2.

——, and H. E. Willoughby, 1982: The response of balanced hurricanes to local sources of heat and momentum. *J. Atmos. Sci.*, **39**, 378–394, doi:10.1175/1520-0469(1982)039<0378:TROBHT>2.0.CO;2.

Sitkowski, M., and G. M. Barnes, 2009: Low-level thermodynamic, kinematic, and reflectivity fields of Hurricane Guillermo (1997) during rapid intensification. *Mon. Wea. Rev.*, **137**, 645–663, doi:10.1175/2008MWR2531.1.

Smith, R. K., and M. T. Montgomery, 2016: The efficiency of diabatic heating and tropical cyclone intensification. *Quart. J. Roy. Meteor. Soc.*, **142**, 2081–2086, doi:10.1002/qj.2804.

——, G. Kilroy, and M. T. Montgomery, 2015: Why do model tropical cyclones intensify more rapidly at low latitudes? *J. Atmos. Sci.*, **72**, 1783–1804, doi:10.1175/JAS-D-14-0044.1.

Stevenson, S. N., K. L. Corbosiero, and J. Molinari, 2014: The convective evolution and rapid intensification of Hurricane Earl (2010). *Mon. Wea. Rev.*, **142**, 4364–4380, doi:10.1175/MWR-D-14-00078.1.

Susca-Lopata, G., J. Zawislak, E. J. Zipser, and R. F. Rogers, 2015: The role of observed environmental conditions and precipitation evolution in the rapid intensification of Hurricane Earl (2010). *Mon. Wea. Rev.*, **143**, 2207–2223, doi:10.1175/MWR-D-14-00283.1.

Tang, B., and K. Emanuel, 2010: Midlevel ventilation's constraint on tropical cyclone intensity. *J. Atmos. Sci.*, **67**, 1817–1830, doi:10.1175/2010JAS3318.1.

Tao, C., and H. Jiang, 2015: Distributions of shallow to very deep precipitation–convection in rapidly intensifying tropical cyclones. *J. Climate*, **28**, 8791–8824, doi:10.1175/JCLI-D-14-00448.1.

Vigh, J. L., and W. H. Schubert, 2009: Rapid development of the tropical cyclone warm core. *J. Atmos. Sci.*, **66**, 3335–3350, doi:10.1175/2009JAS3092.1.

Wu, L., S. A. Braun, J. Halverson, and G. Heymsfield, 2006: A numerical study of Hurricane Erin (2001). Part I: Model

verification and storm evolution. *J. Atmos. Sci.*, **63**, 65–86, doi:10.1175/JAS3597.1.

Zagrodnik, J. P., and H. Jiang, 2014: Rainfall, convection, and latent heating distributions in rapidly intensifying tropical cyclones. *J. Atmos. Sci.*, **71**, 2789–2809, doi:10.1175/JAS-D-13-0314.1.

Zawislak, J., H. Jiang, G. R. Alvey III, E. J. Zipser, R. F. Rogers, J. A. Zhang, and S. N. Stevenson, 2016: Observations of the structure and evolution of Hurricane Edouard (2014) during intensity change. Part I: Relationship between the thermodynamic structure and precipitation. *Mon. Wea. Rev.*, **144**, 3333–3354, doi:10.1175/MWR-D-16-0018.1.

Zhang, D.-L., and H. Chen, 2012: Importance of the upper level warm core in the rapid intensification of a tropical cyclone. *Geophys. Res. Lett.*, **39**, L02806, doi:10.1029/2012GL052355.

Zhang, J. A., and E. W. Uhlhorn, 2012: Hurricane sea surface inflow angle and an observation-based parametric model. *Mon. Wea. Rev.*, **140**, 3587–3605, doi:10.1175/MWR-D-11-00339.1.

——, R. F. Rogers, D. S. Nolan, and F. D. Marks Jr., 2011: On the characteristic height scales of the hurricane boundary layer. *Mon. Wea. Rev.*, **139**, 2523–2535, doi:10.1175/MWR-D-10-05017.1.

——, ——, P. Reasor, E. Uhlhorn, and F. D. Marks Jr., 2013: Asymmetric hurricane boundary layer structure from dropsonde composites in relation to the environmental wind shear. *Mon. Wea. Rev.*, **141**, 3968–3984, doi:10.1175/MWR-D-12-00335.1.

Zipser, E. J., 1977: Mesoscale and convective-scale downdrafts as distinct components of squall-line structure. *Mon. Wea. Rev.*, **105**, 1568–1589, doi:10.1175/1520-0493(1977)105<1568:MACDAD>2.0.CO;2.